PCCP

ROYAL SOCIETY OF CHEMISTRY

PAPER

View Article Online
View Journal | View Issue

Check for updates

Cite this: *Phys. Chem. Chem. Phys.*, 2023, **25**, 4872

The *ab initio* potential energy curves of atom pairs and transport properties of high-temperature vapors of Cu and Si and their mixtures with He, Ar, and Xe gases†

Kevin W. Kayang,[a] Alexey N. Volkov, *[a] Petr A. Zhilyaev[b] and Felix Sharipov [c]

The potential energy curves (PECs) for the homonuclear He–He, Ar–Ar, Cu–Cu, and Si–Si dimers, as well as heteronuclear Cu–He, Cu–Ar, Cu–Xe, Si–He, Si–Ar, and Si–Xe dimers, are obtained in quantum Monte Carlo (QMC) calculations. It is shown that the QMC method provides the PECs with an accuracy comparable with that of the state-of-the-art coupled cluster singles and doubles with perturbative triples corrections [CCSD(T)] calculations. The QMC data are approximated by the Morse long range (MLR) and (12-6) Lennard-Jones (LJ) potentials. The MLR and LJ potentials are used to calculate the deflection angles in binary collisions of corresponding atom pairs and transport coefficients of Cu and Si vapors and their mixtures with He, Ar, and Xe gases in the range of temperature from 100 K to 10 000 K. It is shown that the use of the LJ potentials introduces significant errors in the transport coefficients of high-temperature vapors and gas mixtures. The mixtures with heavy noble gases demonstrate anomalous behavior when the viscosity and thermal conductivity can be larger than that of the corresponding pure substances. In the mixtures with helium, the thermal diffusion factor is found to be unusually large. The calculated viscosity and diffusivity are used to determine parameters of the variable hard sphere and variable soft sphere molecular models as well as parameters of the power-law approximations for the transport coefficients. The results obtained in the present work include all information required for kinetic or continuum simulations of dilute Cu and Si vapors and their mixtures with He, Ar, and Xe gases.

Received 24th October 2022,
Accepted 3rd January 2023

DOI: 10.1039/d2cp04981c

rsc.li/pccp

1. Introduction

The flows of high-temperature vapors of metals and semiconductors, as well as their mixtures with other gases are ubiquitous in laser material processing applications, where the laser heating induces material removal, formation of a gaseous plume, and expansion of the plume into a vacuum or background gas. These applications include laser cutting, drilling, and patterning,[1] laser powder-bed fusion additive manufacturing,[2] deposition of functional thin films,[3–5] fabrication of nanoclusters,[6] laser-induced breakdown spectroscopy (LIBS),[7] and studies of photo-induced desorption of volatile species in the space environment.[8]

The plume expansion processes are theoretically studied based on continuum gas dynamics, *e.g.*, ref. 9–13, and kinetic, *e.g.*, ref. 14–21 models. The latter are usually formulated for numerical simulations in the form of the direct simulation Monte Carlo (DSMC) method.[22] The need in the kinetic simulations is justified by high degrees of translational non-equilibrium, when, *e.g.*, a plume expands into a low-density background gas or vacuum. The numerical simulations of gas flows require multiple constitutive

---

[a] *Department of Mechanical Engineering, University of Alabama, 7th Avenue, Tuscaloosa, AL 35487, USA. E-mail: avolkov1@ua.edu*

[b] *Skolkovo Institute of Science and Technology, 121205, Bolshoy Boulevard 30, bld. 1, Moscow, Russia*

[c] *Departamento de Física, Universidade Federal do Paraná, Caixa Postal 19044, Curitiba 81531-980, Brazil*

† Electronic supplementary information (ESI) available: The discussion of the choice of numerical parameters for the quantum Monte Carlo (QMC) calculations which ensures the convergence of the numerical results (Section S1), tables with the atom pair (dimer) energies obtained in the QMC calculations (Section S2), description of the approach used to parameterize the Morse long range (MLR) potential (Section S3), comparison of the QMC potential energy curves (PECs) with available literature data (Section S4), additional plots that characterize the effect of the PEC shape on the scattering of atoms in binary collisions (Section S5), discussion of the choice of the numerical parameters used for calculation of the transport coefficients (Section S6), plots of the major transport collision integrals for various atom pairs and viscosity of noble gases (Section S7), plots that characterize the effect of the LJ and VSS approximations on the transport coefficients of the Cu–Ar mixture (Section S8), and description of additional supplementary text files containing the tabulated transport coefficients (Section S9). See DOI: **https://doi.org/10.1039/d2cp04981c**

relations that describe the transport processes such as diffusion, viscous drag, and heat conduction. For kinetic simulations of dilute monatomic gases based on the Boltzmann kinetic equation and its generalizations, the necessary constitutive relations include the differential collision cross section as a function of the deflection angle and relative velocity.[23–25] The DSMC treatment of collisions is usually based on molecular collision models, such as the hard sphere (HS), variable hard sphere (VHS),[26] and variable soft sphere (VSS)[27] models, which determine the differential collision cross section and contain only a few adjustable parameters. For continuum simulations of dilute monatomic gases based on the Navier–Stokes equations, the required relations include diffusivity, shear viscosity, and thermal conductivity of pure gas substances and gas mixtures as functions of gas temperature, density, and molar fractions of species.[23–25]

The collisional and transport properties are currently well-known for noble gases, components of the atmospheric air, and some other species that exist in a gaseous form at room temperature. The properties of high-temperature vapors of metals and semiconductors, including the parameters of the VHS and VSS molecular models, are currently known with much less accuracy or not known at all.[28,29] In particular, the molecular model parameters remain unknown for multiple cross-species collisions involving a vapor atom and atom of a background gas.

The transport processes in dilute gases are ultimately defined by the momentum and energy exchange during binary collisions between gas particles. If the gas temperature is sufficiently high, the quantum effects in interaction between atoms in the ground state are small.[24,25] For example, for argon, the quantum effects in binary collisions change the viscosity in $\sim$0.15% at a temperature of 50 K and in less than 0.1% when the temperature is equal to or greater than 120 K.[30] Then the solution of the classical scattering problem, *e.g.*, ref. 23–31, can be used to calculate the deflection angle in binary collisions and, consequently, transport coefficients of pure gas substances and gaseous mixtures using the Chapman–Enskog method based on interatomic potentials or potential energy curves (PECs) for corresponding atom pairs.[23–25] The VHS and VSS model parameters can be also directly derived from the PECs using the Chapman–Enskog method.[22,32] The approach to sampling interatomic collisions in the DSMC method can also be directly based on the solution of the classical scattering problem that uses PECs as an input for the calculation of the outcome of each binary collision in the course of a DSMC simulation.[33,34]

The present paper is targeted at filling the gap in understanding of the collisional and transport properties of high-temperature vapors and their mixtures with noble gases, which are calculated here based on PECs for corresponding dimers or atom pairs established in high-fidelity *ab initio* calculations (hereinafter, when discussing PECs, the terms ''dimer'' and ''atom pair'' are used interchangeably since the *ab initio* PECs for dimers in the ground state can be further used to calculate collisions between corresponding pairs of atoms). For this purpose, we first obtain the PECs for atom pairs of interest in the quantum Monte Carlo (QMC) calculations for a broad range of interatomic distances. Second, we investigate the collisional and transport properties of high-temperature vapors of copper and silicon, as well as their mixtures with helium, argon, and xenon gases from first principles. Finally, we present the obtained results in the approximate form of VHS and VSS molecular models that can be readily used in kinetic and continuum simulations of corresponding gas flows.

Copper and silicon are chosen for investigation due to the tremendous practical importance of these materials and, correspondingly, large amounts of experimental and computational studies involving laser-, ion spattering-, and plasma etching-induced flows of Cu or Si vapor plumes, *e.g.*, ref. 35–38. The simultaneous consideration of light-weight He, medium-weight Ar, and heavy Xe gases is inspired by the results of recent experimental[39] and computational studies[17,19] that report the strong effect of the molecular weight of a noble background gas on the plume or jet expansion processes in material processing technologies. The transport properties of Cu and Si vapors are of practical interest at elevated temperatures, *e.g.*, roughly from 2000 K to 6000 K at atmospheric pressure. The condensation processes limit the lower temperature, while the upper temperature is limited by ionization. The exact temperature range, where the gas–vapor mixtures can exist in the form of mixtures of neutral monatomic gases, depends on pressure and degree of flow non-equilibrium. Under conditions of strongly non-equilibrium flows, the neutral atoms can exist in a broader range of conditions compared to equilibrium. Therefore, the transport properties are considered in the present paper in the extended range of temperature from 10^2 K to 10^4 K.

Currently, the *ab initio* PECs are known with very high accuracy for homonuclear and heteronuclear dimers of noble gases, *e.g.*, ref. 40–48. These PECs are often approximated by the Tang & Toennies[49,50] potential or its generalized versions, *e.g.*, by the universal potential recently suggested in ref. 51, and are used for high-fidelity calculations of the collisional and transport properties of corresponding gases and gaseous mixtures, *e.g.*, ref. 30, 47 and 52–57. These calculations show a good agreement between the predicted and experimentally measured viscosities.[58] In the literature, the *ab initio* or experimental PECs can be also found for the Cu–Cu,[20,59–61] Cu–He,[62,63] Cu–Ar,[62] Si–Si,[64] and Si–Ar[65] dimers (hereinafter, the notation ''A–B'' is used for the dimer formed by atoms A and B, pair of atoms A and B whose binary collision is under consideration, and gas mixture composed of monatomic gases A and B). These data, however, are partially incomplete since the data points often do not cover a sufficiently large range of interatomic distance.

Most of the calculations of dimer PECs mentioned above are performed based on the coupled cluster singles and doubles with perturbative triples corrections [CCSD(T)] method,[66] which is considered as a state-of-the-art approach for high-fidelity calculations of PECs. This method, however, is characterized by high computational costs that scale as N_e^7 where N_e is the number of electrons. The density functional theory (DFT)[67] is rarely used for calculations of dimer PECs, as the approximate energy functionals used in the DFT calculations require additional corrections for van der Waals interactions and can either underpredict or overpredict the potential energy well depth.[68] Moreover, the PECs obtained in the DFT calculations have been reported to break down in the attraction parts with the relative errors in the ground-state energy strongly increasing with increasing interatomic distance.[69,70] These limitations of DFT are overcome in the QMC method,[71–73] which uses stochastic techniques to sample wave functions in the quantum many-body problem. Compared to DFT, the QMC method does not require further approximations to account for van der Waals interactions.[71,74] Providing the same level of accuracy as the post-Hartree–Fock methods such as CCSD(T), the QMC method is less computationally demanding, as its computational cost scales as N_e^3. At the same time, as a stochastic approach, the QMC method usually requires a generation of large-size statistical samples.[71]

In the present work, the PECs for the homonuclear He–He, Ar–Ar, Cu–Cu, and Si–Si dimers, as well as heteronuclear Cu–He, Cu–Ar, Cu–Xe, Si–He, Si–Ar, and Si–Xe dimers, are determined in the QMC calculations using the QMCPACK package[75,76] and then approximated by the Morse long range[77,78] (MLR) and Lennard-Jones (LJ) potentials (Section 2). For the Xe–Xe dimer, the MLR and LJ approximations are obtained based on the results reported in ref. 48. Then the obtained MLR and LJ potentials are used to calculate the deflection angle at binary collisions of atoms in Section 3, as well as transport coefficients of pure vapors of Cu and Si and their mixtures with He, Ar, and Xe gases based on the ten-term approximations with respect to the Sonine polynomials of the Chapman–Enskog theory (Sections 4–6). The obtained values of viscosity and diffusivity are used to find parameters of the VHS and VSS molecular models for kinetic simulations and power-law approximations of the transport coefficients as functions of temperature for continuum simulations in Section 7. Finally, the major results of this study are summarized in Section 8. The raw results of calculations of the PECs, deflection angles, transport collision integrals, and transport coefficients are provided in the form of tables, plots, and text files in the Appendix and ESI.†

2. Potential energy curves (PECs)

2.1. Quantum Monte Carlo (QMC) calculations of PECs

The QMC calculations of PECs were conducted with the QMCPACK package.[75,76] We used the trial wave functions of the Slater–Jastrow type, $\boldsymbol{\Psi}_{\mathbf{T}} = \boldsymbol{e}^{\boldsymbol{J}}\boldsymbol{D}_{\uparrow}\boldsymbol{D}_{\downarrow}$, where $\boldsymbol{D}_{\uparrow}$ and $\boldsymbol{D}_{\downarrow}$ are the Slater determinants of the spin-up and spin-down electrons respectively and $\boldsymbol{J}$ is the Jastrow factor. This form of the trial wave functions was chosen because it has a general form and was applied to many electronic systems ranging from single atoms to many-atom solids.[71] The Slater determinants are constructed based on the Kohn–Sham (KS) DFT orbitals obtained using the QUANTUM ESPRESSO package.[79,80]

In setting up the DFT calculations, the self-consistent field (scf) calculations were performed in a sample periodic box of 20 Å × 20 Å × 20 Å which is large enough to make the interactions of atoms through periodic boundaries negligible. The local density approximation (LDA) was used to approximate the exchange–correlation functional.[81]

The trial wave function constructed from the KS orbitals is firstly optimized using the variational Monte Carlo (VMC) scheme in the QMCPACK package. The statistical error estimates of the VMC scheme are further minimized by adjusting the trial wave functions. For this purpose, a large cut-off energy and special QMC-type pseudo-potentials are applied. As such, the plane-wave cut-off energy was set to 5440 eV (400 Ry) since the preliminary calculations showed that increasing the plane-wave cutoff energy did not significantly change the resulting energy. The norm-conserving plane-wave pseudopotentials parameterized by Burkatzki, Filippi, and Dolg were also used[82,83] since these pseudopotentials were generated specifically for subsequent QMC calculations and have been shown to produce more accurate trial wave functions unlike other general pseudopotentials which can produce time-step errors in the diffusion Monte Carlo (DMC) scheme.[84]

The calculations are performed for isolated atoms and dimers in the ground states (Table 1). The values of numerical parameters, including the plane-wave cutoff energy in the DFT calculations, number of samples and wavefunction optimization cycles in VMC calculations, DMC timestep, and number of DMC walkers, are chosen in a preliminary convergence study. This convergence study ensures statistical convergence and good computational accuracy of the QMC calculations, which is especially important for dimers characterized by small potential well depth, such as the He–He dimer. Based on the results of the convergence study, the number of statistical samples ranging from 12 800 to 51 200 was used in the simulations. The number of the VMC optimization cycle was equal to 9. The DMC calculations were performed using 128 to 256 random walkers, with the DMC walkers being initialized from the VMC random walk, with a time step of 0.005 a.u.[85]

The potential energy V was then computed as $V = V_{12} - (V_1 + V_2)$, where V_{12} is the dimer energy, and V_k are the energies of isolated atoms ($k = 1, 2$). Overall, the QMC calculations were performed for pairs of atoms with interatomic distances r ranging from 0.4–1 Å to 10 Å. The smallest value of r was chosen individually for each dimer to ensure that the investigated range of r is sufficient for high-fidelity calculations of the gas transport coefficients up to a temperature of 10^4 K.

The tabulated values of energy obtained in the QMC calculations for all dimers under consideration are provided in the Appendix.[85] For each dimer, the values of the potential well depth (binding energy) D_e and equilibrium interatomic distance r_e are calculated by means of the three-point interpolation of the PEC established in the QMC calculations. For this

Table 1 Valence electronic configurations and masses[94] m_k of atoms considered in calculations

Element	He	Ar	Xe	Cu	Si
Configuration	$1s^2$	$3s^2\ 3p^6$	$4d^{10}\ 5s^2\ 5p^6$	$3d^{10}\ 4s^1$	$3s^2\ 3p^2$
Mass m_k (Da)	4.002602	39.948	131.293	63.546	28.0855

Table 2 Potential well depths D_e and equilibrium distances r_e for various dimers obtained in the present work and available from the literature

Dimer	D_e (eV)	r_e (Å)	Ref[a]	Method of calculation or "Exp." for experimental values
He–He	9.461×10^{-4}	2.969	This work	QMC[b]
	9.4514×10^{-4}	2.9676	47 (51)	Post-Hartree–Fock, CCSD(T)
	9.4798×10^{-4}	2.9634	44	Post-Hartree–Fock, CCSD(T)[c]
	9.4428×10^{-4}	2.9634	42 (50)	QMC
Ar–Ar	0.01225	3.770	This work	QMC
	0.0127	3.754	20	DFT-vdW[d]
	0.01233	3.762	45	Post-Hartree–Fock, CCSD(T)
	0.0123	3.75	46	Post-Hartree–Fock, CCSD(T)
	0.01235	3.7572	41 (50)	Hartree–Fock, HFDID1[e]
	0.0123	3.761	86	Exp.
	0.0107	3.727	24	Exp., parameters of the LJ potential based on the viscosity data
Xe–Xe	0.02408	4.3779	48 (51)	Post-Hartree–Fock CCSD(T)
	0.02408	4.3779	48	Post-Hartree–Fock CCSD(T)
	0.02438	4.3657	40 (50)	Hartree–Fock, HFD-B[f]
Cu–Cu	2.192	2.2	This work	QMC
	2.166	2.175	20	DFT-vdW
	2.22	1.9169	61	Post-Hartree–Fock CCSD(T)
	2.021	2.214	60	Post-Hartree–Fock, CCSD(T)
	2.203	2.274	59	Post-Hartree–Fock, APUMP4[g]
	2.2	1.98408	87	Exp.
	2.038	2.22	88,89	Exp.
Si–Si	3.257	2.278	This work	QMC
	3.2527	2.273	64	Post-Hartree–Fock, CCSD(T)
Cu–He	8.192×10^{-4}	4.616	This work	QMC
	8.2123×10^{-4}	4.662	63	Post-Hartree–Fock, CCSD(T)
	7.728×10^{-4}	4.56	62	Post-Hartree–Fock, CCSD(T)
Cu–Ar	0.01013	4.039	This work	QMC
	0.01009	4.032	63	Post-Hartree–Fock, CCSD(T)
Si–Ar	3.690×10^{-2}	3.365	This work	QMC
	3.6672×10^{-2}	3.386	65	Post-Hartree–Fock, RUCCSD(T)[h]

[a] In the secondary references given in parenthesis, the computational data from the corresponding primary references are used to develop functional forms of PECs. [b] QMC – Quantum Monte Carlo. [c] CCSD(T) – Coupled cluster singles and doubles with perturbative triples corrections. [d] DFT-vdW – Density functional theory with van der Waals corrections. [e] HFDID1 – Hartree–Fock dispersion individually damped potential. [f] HFD-B – Hartree–Fock dispersion. [g] APUMP4 – Approximate projected unrestricted Møller–Plesset to 4th order. [h] RUCCSD(T) – Spin unrestricted open-shell coupled cluster singles and doubles with perturbative triples corrections.

purpose, three QMC data points with the minimum values of energy are used.

To validate the QMC computational approach, the calculated values of D_e and r_e are compared in Table 2 with the literature data, obtained both in computations, using various simulation techniques, and in the experiments reported in ref. 86–89. Table 2 also contains D_e and r_e for the Xe–Xe dimer, whose PEC was not calculated in the present work. The comparison shows that the results of our calculations of D_e and r_e agree very well with the most recent values obtained in the CCSD(T) calculations and, in some cases, with the calculations based on other *ab initio* approaches. With a few exclusions, the values of D_e and r_e predicted by different computational approaches or experimentally are consistent with each other. The PECs for the He–He and Ar–Ar dimers obtained in various works are compared with the results from the present calculations in Fig. 1.[85]

2.2. PECs of the He–He, Ar–Ar, and Xe–Xe dimers

As the PECs for noble gases are well-known from the CCSD(T) calculations, the corresponding PECs are calculated in the present work to reveal the capability of the QMC method to accurately predict PECs in a broad range of r as well as to validate the approaches for the parameterization of PECs in a functional form and calculation of the transport coefficients.

In Fig. 1, the calculated values of PECs for the noble gas dimers He–He and Ar–Ar (squares) are compared with the values obtained in ref. 44 and 45 (crosses). The comparison shows close agreement between the results of the QMC and CCSD(T) calculations in the whole ranges of r. The difference between the values of D_e and r_e computed is less than 0.2% for the He–He dimer and 0.06% for the Ar–Ar dimer.

Based on the good agreement between the results of our QMC calculations and CCSD(T) calculations from the literature for the He–He and Ar–Ar dimers, we decided not to perform the QMC calculations for the Xe–Xe dimer and to use the PEC suggested in ref. 48 in the functional form of the Tang & Toennies potential,[49] where the parameters are chosen to fit the energy values obtained in the CCSD(T) calculations.[85]

2.3. PECs of the Cu–Cu, Cu–He, Cu–Ar, and Cu–Xe dimers

The energy values obtained in the QMC calculations for the homonuclear Cu–Cu dimer are shown by symbols in Fig. 2(a). The calculated values of D_e and r_e are consistent with the values obtained based on other *ab initio* computational approaches[20,59–61] with the typical differences on the order of 1% to 10% (Table 2). In particular, the present calculations provide D_e and r_e that are less than 1.5% different from those that are found in the DFT calculations,[20] where the long-range van der Waals interactions are accounted for based on the Grimme's D2 correction.[90]

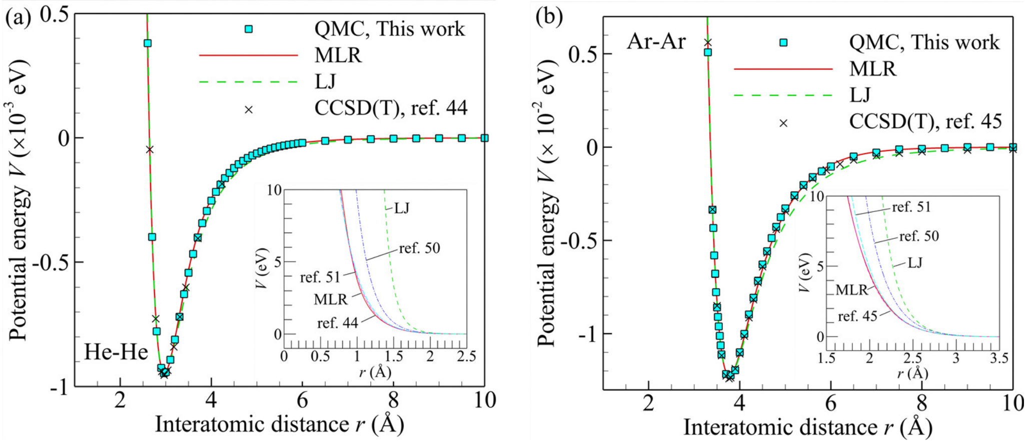

Fig. 1 Potential energy of the homonuclear He–He (a) and Ar–Ar (b) dimers. The red squares show the calculated QMC values, the crosses represent the values of energy for the He–He dimer taken from ref. 44 and Ar–Ar dimer from ref. 45 obtained in the CCSD(T) calculations, and the solid and dashed curves are the approximations of the QMC values by the MLR and LJ potentials, respectively. The insets show various functional approximations of PECs in the ranges of r corresponding to large repulsive energies: MLR (red solid curves) and LJ (green dashed curves) potentials obtained in the present work, potentials from ref. 50 (blue dashed-dotted curves), ref. 44 [for He–He in (a)] and ref. 45 [for Ar–Ar in (b)] (magenta dashed-double-dotted curves), and ref. 51 (cyan long-dashed curves). In both insets, the curves corresponding to the MLR potentials and potentials suggested in ref. 44 in (a) and ref. 45 in (b) visually coincide with each other.

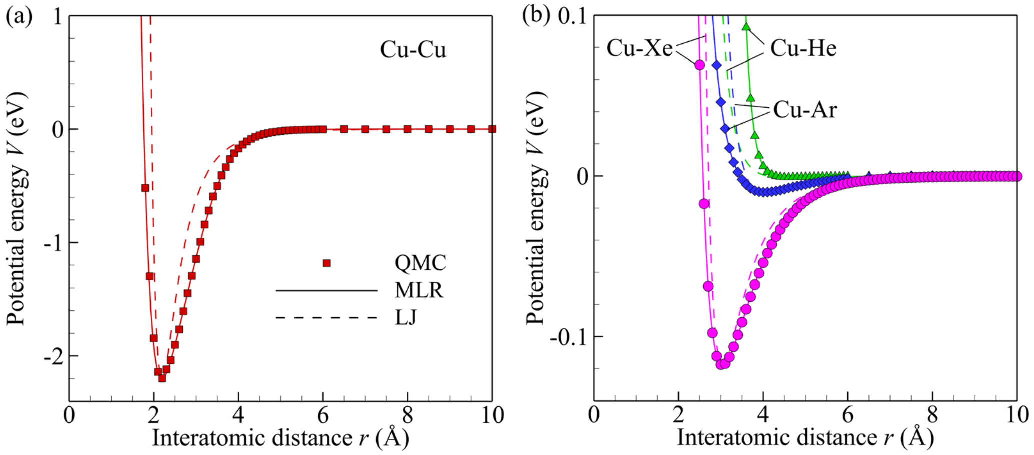

Fig. 2 Potential energy of the homonuclear Cu–Cu dimer (squares and red curves) (a) as well as heteronuclear Cu–He (triangles and green curves), Cu–Ar (diamonds and blue curves), and Cu–Xe (circles and magenta curves) dimers (b). The symbols correspond to the values found in the QMC calculations, while the solid and dashed curves are approximations of the QMC values by the MLR and LJ potentials, respectively.

The energy values obtained in the QMC calculations for heteronuclear dimers that include a Cu atom and a noble gas atom are shown by symbols in Fig. 2(b). The binding energies of such dimers are strongly reduced compared to the Cu–Cu dimer and have an order of magnitude of D_e for the corresponding homonuclear noble gas dimers. This agrees with the analysis of PECs of the Cu–He and Cu–Ar dimers obtained in the CCSD(T) calculations and suggests a weak, van der Waals-type bonding between the metal and noble gas atoms.[62,63] The potential well depth monotonically increases while the equilibrium distance monotonically decreases with an increasing atomic number of the noble gas atom. The same trends were found for a series of dimers of a Cu atom with He, Ne, and Ar atoms.[63] This was attributed to the difference in the principal quantum number of noble gas atoms, which affect the distributions of the wave functions of electrons in the outermost shell such that, when a Cu atom and noble gas atom are at an equilibrium distance, the overlapping portions of the wave functions increase with the increasing number of electrons in the noble gas atom.

2.4. PECs of the Si–Si, Si–He, Si–Ar, and Si–Xe dimers

The values of energy found in the QMC calculations for the homonuclear Si–Si dimer are shown by symbols in Fig. 3(a). The results obtained in the present work are in close quantitative agreement with the results of CCSD(T) calculations both in terms of D_e and r_e (Table 2) and the whole PEC.[85]

The calculated PECs for the heteronuclear Si–He, Si–Ar, and Si–Xe dimers [Fig. 3(b)] demonstrate similar trends which are revealed for heteronuclear dimers containing a Cu atom:

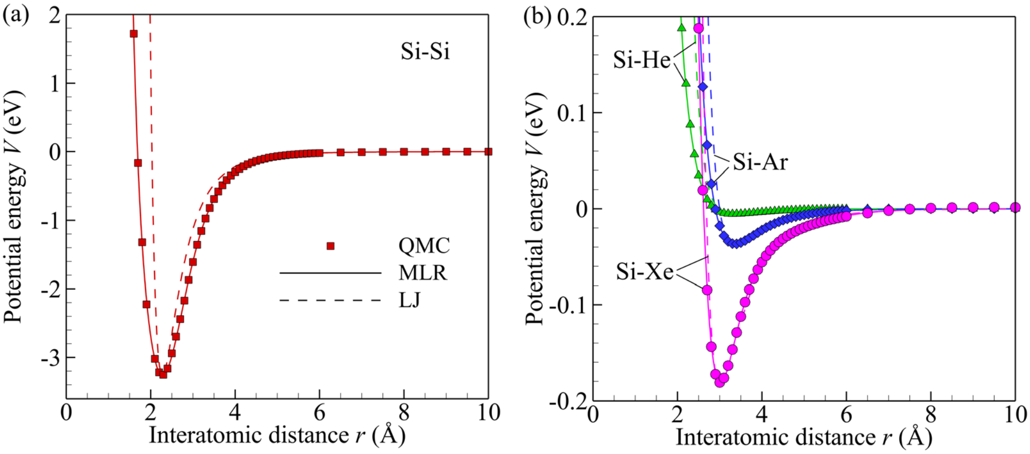

Fig. 3 Potential energy of the homonuclear Si–Si dimer (squares and red curves) (a) as well as heteronuclear Si–He (triangles and green curves), Si–Ar (diamonds and blue curves), and Si–Xe (circles and magenta curves) dimers (b). The symbols correspond to the values found in the QMC calculations, while the solid and dashed curves are approximations of the QMC values by the MLR and LJ potentials, respectively.

The binding energies are small, which suggests dispersive interaction between atoms in these dimers, and D_e monotonically increases with an increasing atomic number of the noble gas atom. Contrary to the case of the Cu–A dimers, the variation of r_e for the Si–A dimers is non-monotonous with respect to the mass of atom A, as the r_e for the Si–He dimer is in between the equilibrium distances for the Si–Ar and Si–Xe dimers. The difference in r_e between the Si–He and Si–Ar dimers, however, is only ~1%. Interestingly, the slope of the repulsive part of the Si–He PEC, when r is moderately different from r_e, is much smaller than that for the Si–Ar and Si–Xe dimers, so that the repulsive part of the Si–He interatomic potential is much softer than its Si–Ar and Si–Xe counterparts. The computed values of D_e and r_e for the Si–Ar dimer are only less than 0.5% different from the corresponding values found in the calculations based on the spin unrestricted open-shell coupled cluster singles and doubles with perturbative triples corrections method.[65]

2.5. Morse long range (MLR) and Lennard-Jones (LJ) approximations of PECs

Various functional forms of interatomic potentials are currently available for approximation of *ab initio* PECs depending on the bonding type and other factors, *e.g.*, ref. 91. Here, we use the Morse long-range (MLR) potential function[77,78] as a convenient model that allows us to accurately approximate the QMC data points for dimers with different types of bonding, including van der Waals, metallic, and covalent bonding.

The PECs obtained in the QMC calculations are approximated by the MLR potential in the form

$$V(r) = D_e\left(1 - \frac{u(r)}{u(r_e)}e^{-\beta(r)y(r)}\right)^2 - D_e, \tag{1}$$

where r is the interatomic distance and $u(r)$ is a three-term function describing the long-range behavior of the PEC:

$$u(r) = \frac{C_6}{r^6} + \frac{C_8}{r^8} + \frac{C_{10}}{r^{10}}, \tag{2}$$

$$\beta(r) = y(r)\beta_\infty + [1 - y(r)]\sum_{i=0}^{4}\beta_i y(r)^i, \tag{3}$$

$$y(r) = \frac{r^3 - r_e{}^3}{r^3 + r_e{}^3}, \tag{4}$$

$$\beta_\infty = \ln(2D_e/u(r_e)). \tag{5}$$

Besides D_e and r_e, this potential has eight interpolating parameters C_6, C_8, C_{10}, β_0, β_1, β_2, β_3, and β_4. The values of D_e and r_e are calculated as the parameters at the minimum of the three-point interpolation of the PEC established in the QMC calculations, as discussed in Section 2.1. The remaining parameters C_6, C_8, C_{10}, β_0, β_1, β_2, β_3, and β_4 are calculated by multifactorial non-linear least-square fitting that minimizes the relative root-mean-square (RMS) deviation

$$\mathrm{RMS} = \left(\frac{1}{N}\sum_{i=1}^{N}\Delta_i^2\right)^{1/2}, \tag{6}$$

where $\Delta_i = [V(r_i) - V_{\mathrm{QMC}(i)}]/V_{\mathrm{QMC}(i)}$,$V_{\mathrm{QMC}(i)}$ is the potential energy found in the QMC calculations at $r = r_i$, and all N data points with $r = r_i$ belongs to a range $r_{\mathrm{f,min}} \le r \le r_{\mathrm{f,max}}$. The boundaries of this range are chosen individually for each dimer to ensure that the MLR potential has only one extremum at $r = r_e$ and $r_{\mathrm{f,min}}$ is small enough to enable accurate calculations of transport coefficients at temperatures $T \le T_{\max} = 10^4$ K.[85]

The obtained parameters of the MLR potentials for all dimers under consideration are presented in Table 3. The values of the relative RMS deviation for most dimers span the range from ~0.5% to ~3% but approach 5% for the Ar–Ar and Cu–Cu dimers. The parameters of the MLR potential for the Xe–Xe dimer are calculated by the least-square fitting of the Tang & Toennies-type[49] potential function obtained in ref. 48.[85] The corresponding potentials are shown by solid curves in Fig. 1–3. As seen in Fig. 1, the developed MLR potentials for the He–He and Ar–Ar dimers agree well with the potential functions developed in ref. 44, 45, and 51. The potential

Table 3 Parameters of the MLR and LJ potentials obtained by fitting the QMC PECs calculated in the present work. RMS is the relative RMS deviation of the MLR potentials from the QMC data points calculated based on eqn (6). The potential parameters for the Xe–Xe dimer are calculated by fitting the PEC in the functional form obtained in ref. 48

Dimer	D_e (eV)	r_e (Å)	C_6 (eV Å^6)	C_8 (eV Å^8)	C_{10} (eV Å^{10})	β_0	β_1	β_2	β_3	β_4	RMS
He–He	9.461×10^{-4}	2.969	4.019×10^{-1}	-2.488×10^{-1}	4.274×10^{-2}	2.648×10^{-1}	2.119×10^{-1}	-3.450×10^{-1}	-2.522	-2.914	3.29×10^{-2}
Ar–Ar	1.225×10^{-2}	3.770	2.003	-2.815	1.153	2.785×10^{-1}	-2.602	-3.036	-3.319	-2.453	4.80×10^{-2}
Xe–Xe	2.406×10^{-2}	4.378	1.302×10^{2}	-2.699×10^{2}	1.680×10^{2}	3.875×10^{-1}	4.201×10^{-1}	-6.258×10^{-2}	-6.589×10^{-1}	-1.056	4.76×10^{-3}
Cu–Cu	2.200	2.192	2.017×10^{1}	-1.283×10^{1}	2.290	-1.530	-4.766	-5.815	-4.145	-1.491	4.18×10^{-2}
Cu–He	8.192×10^{-4}	4.616	3.043	-1.672×10^{1}	2.880×10^{1}	2.059	-3.771	-4.593	-1.542	7.245×10^{-1}	2.09×10^{-2}
Cu–Ar	1.013×10^{-2}	4.039	4.194×10^{-2}	-2.574×10^{-1}	6.916×10^{-1}	-2.019×10^{-1}	-6.768	-7.384	-9.995	-6.909	1.27×10^{-2}
Cu–Xe	1.177×10^{-1}	3.040	6.107×10^{1}	-6.155×10^{1}	1.887×10^{1}	-9.486×10^{-1}	-1.666	-1.258	-1.233	-1.361	4.38×10^{-3}
Si–Si	3.257	2.278	7.998×10^{2}	-9.943×10^{2}	3.790×10^{2}	-1.565	-1.418×10^{-1}	9.702×10^{-1}	-1.120×10^{-1}	-9.960×10^{-1}	9.08×10^{-3}
Si–He	5.402×10^{-3}	3.330	1.328	-8.725	1.744×10^{1}	1.601×10^{-1}	-3.401	-1.709	-2.573×10^{-1}	-2.239	1.84×10^{-2}
Si–Ar	3.690×10^{-2}	3.365	1.982×10^{1}	-1.129×10^{2}	2.959×10^{2}	3.213×10^{-3}	-7.546×10^{-1}	-9.259×10^{-1}	-3.060	-3.882	1.71×10^{-2}
Si–Xe	1.812×10^{-1}	3.015	2.915×10^{1}	-1.478×10^{2}	2.524×10^{2}	6.561×10^{-1}	7.387×10^{-2}	-2.786×10^{-1}	-9.599	-1.294×10^{1}	2.87×10^{-2}

function for the noble gas dimers suggested in ref. 50 significantly overestimates the potential energy at small interatomic distances that correspond to strong repulsive interaction.

The (12-6) Lennard-Jones (LJ) potential in the form

$$V(r) = D_e\left[\left(\frac{r_e}{r}\right)^{12} - 2\left(\frac{r_e}{r}\right)^{6}\right], \tag{7}$$

is still a popular approximation for the calculation of the collisional and transport properties of high-temperature gases and vapors, especially under conditions when the exact PEC is not available.[29] For noble gases, this potential is known to provide an approximation of PECs that is sufficient for kinetic simulations of gas flows at moderate temperatures[92] and calculation of transport properties in agreement with experimental viscosity data.[24] Since the LJ potential is widely used, it is important to quantify the errors in the transport coefficients of high-temperature vapors and gaseous mixtures imposed by the use of this potential function. Various generalizations of the LJ potential, *e.g.*, improved LJ (ILJ) potential,[93] offer potentially better accuracy compared to (12-6) LJ potential at the price of at least one additional fitting parameter. Since these parameters can be determined only based on known *ab initio* PECs or spectroscopical measurements, these generalized LJ potentials do not have a decisive advantage over more complex potential functions, *e.g.*, the MLR potential adopted in the present work.

To verify the applicability of the LJ potential for the homonuclear Cu–Cu and Si–Si dimers as well as for the heteronuclear dimers, the values of the LJ potentials with D_e and r_e from Table 3 are plotted by dashed curves in Fig. 1–3. The relative RMS deviations of the LJ potentials are 1–3 orders of magnitude larger than that of the corresponding MLR potentials.[85]

As expected, the LJ potentials provide reasonably good approximations of the actual PECs for the noble gas dimers at $r \gtrsim r_e$. At interatomic distances that correspond to strong repulsion, however, the LJ potentials strongly overestimate both energy and force (insets in Fig. 1). As shown in Sections 5.1, 5.2 and 6.3, this results in relatively large errors in the values of the transport coefficients of noble gases and their mixtures with Cu vapor at large temperatures. It makes the LJ potential not a suitable approximation for high-fidelity simulations of high-temperature flows of pure substances and gas mixtures considered in the present work.

For the homonuclear Cu–Cu and Si–Si dimers, the LJ potentials strongly overestimate the energy and interatomic interaction force at both attraction and repulsion [Fig. 2(a) and 3(a)]. As shown in ref. 20, a generalized (*m*-*n*) Lennard-Jones potential, where the exponents *m* and *n* are chosen to exactly fit the zero energy point and potential stiffness at $r = r_e$ can substantially improve the accuracy of the approximation of the Cu–Cu PEC only in a small vicinity of $r = r_e$, in the range from ∼1.7 Å to ∼2.7 Å, but still provides insufficient accuracy outside this range.

For the heteronuclear dimers, the LJ potentials, as a rule, strongly overestimate the energy and force at $r < r_e$ [Fig. 2(b) and 3(b)]. For the Cu–He dimer, however, the LJ potential underestimates the energy and force. This also suggests that the LJ approximations of the PECs for all heteronuclear dimers under consideration must not be used for calculations of the collisional and transport properties of corresponding gas mixtures at high temperatures.

3. Effect of the PEC shape on particle scattering in binary collisions

To solve the Boltzmann kinetic equation for monatomic gases, the deflection angle χ, *i.e.*, the angle between the relative velocity vectors of colliding particles before and after a binary collision, must be determined based on $V(r)$. Here, the solution of the classical elastic scattering problem[22–25,31] is used to find χ as a function of the magnitude of the relative particle velocity before the collision C_r and geometrical collision parameter b in the form:

$$\chi(C_r, b) = \pi - \int_{r_{\min}}^{\infty} \frac{L_r \mathrm{d}r}{mr^2\sqrt{\dfrac{H_r - V(r)}{2m} - \dfrac{L_r^2}{(2mr)^2}}}, \tag{8}$$

where $m = m_1m_2/(m_1 + m_2)$ is the reduced mass for interacting particles with masses m_1 and m_2 (Table 1),[94] $V(r)$ is the PEC for participating particle species, $H_r = mC_r^2/2$, $L_r = mC_rb$, and $r_{\min}$ is the minimum distance between particles attained at a collision which can be found as the largest root of the equation

$$\frac{H_r - V(r_{\min})}{2m} = \frac{L_r^2}{(2mr_{\min})^2}. \tag{9}$$

In the present work, the tables of values of $\chi_{ij} = \chi(b_j, C_{ri})$ (the scattering matrices) are calculated for all atom pairs in the ranges $0 \leq b \leq 20$ Å and $0 < C_r \leq C_{r*}$, where the values of C_{r*} were chosen in preliminary calculations individually for each pair of atoms to ensure the accuracy of further calculation of the transport coefficients up to $T = 10^4$ K.[85] The integral in eqn (8) was calculated numerically, assuming that the atoms do not interact with each other when r is greater than the cutoff distance $r_{\text{cutoff}} = 40$ Å. Then the range $r \geq r_{\min}$ was divided into 3 sub-ranges: $r_{\min} + 10^{-7}$ Å $\leq r \leq 10^{-4}$ Å (range I), 10^{-4} Å $\leq r \leq r_{\text{cutoff}}$ (range II), and $r \geq r_{\text{cutoff}}$ (range III), where the lower boundary in range I is shifted with respect to $r_{\min}$ to exclude the singularity at $r = r_{\min}$. The numerical integration in ranges I and II is performed with the simple trapezoidal rule and spacings $\Delta r = 10^{-7}$ Å and $\Delta r = 10^{-4}$ Å, respectively, while the contribution of range III is calculated as $\Delta\chi_{\text{III}} = 2\arcsin(b/r_{\text{cutoff}})$.

The tables of the deflection angle are calculated for all atom pairs under consideration.[95] The characteristic distributions of the quantity $\vartheta = 1 - \cos\chi$ *versus* b^2 for single-species collisions in the Ar–Ar and Cu–Cu atom pairs as well as cross-species collisions in the Cu–He atom pair, calculated based on the MLR and LJ potentials are shown in Fig. 4–6 by solid and dashed curves, respectively. The similar plots for all other atom pairs under consideration are presented in the ESI.† At relatively small C_r, the plots, *e.g.*, in Fig. 4(a), show two characteristic ranges of b, the first one for nearly head-on collisions, which are primarily controlled by the interatomic repulsion, and the second for quasi-orbiting collisions, which are strongly affected by attraction. With increasing C_r, the contribution of quasi-orbiting collisions becomes almost negligible and invisible on the scale of Fig. 4–6.

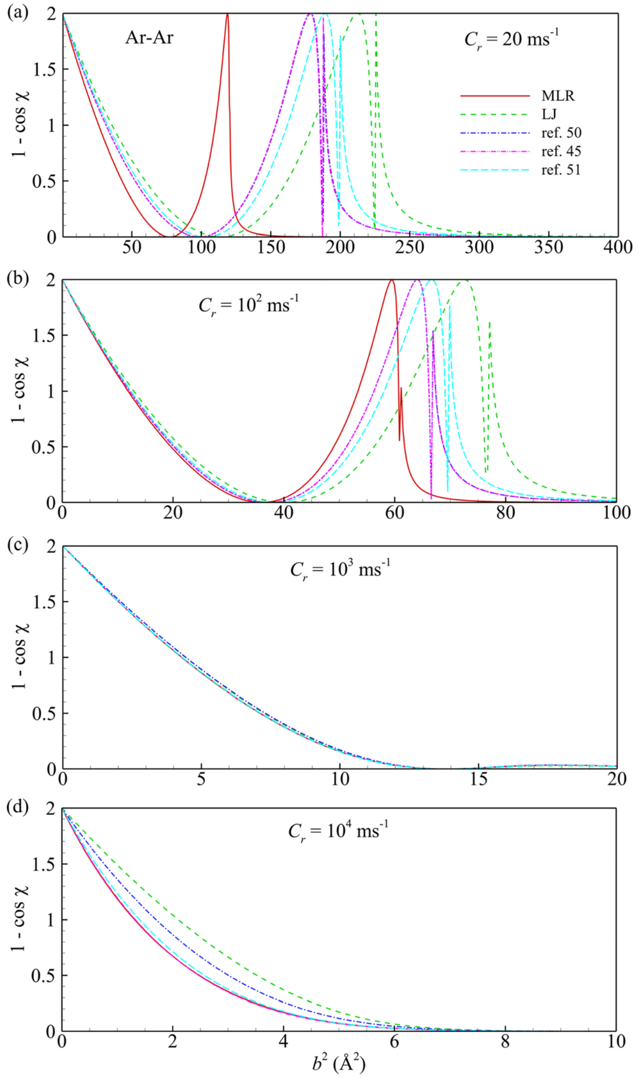

Fig. 4 Quantity $1 - \cos\chi$, where χ is the deflection angle defined by eqn (8), *versus* b^2 for two Ar atoms at a relative speed C_r of 20 m s^{-1} (a), 10^2 m s^{-1} (b), 10^3 m s^{-1} (c), and 10^4 m s^{-1} (d) calculated based on the MLR (red solid curves) and LJ (greed dashed curves) potentials as well for the PECs in the functional forms suggested in ref. 50 (blue dashed-dotted curves), ref. 45 (magenta dashed-double-dotted curves), and ref. 51 (cyan long-dashed curves).

For all atom pairs, the values of ϑ calculated based on the LJ potentials demonstrate the strongest deviation from the values of ϑ calculated based on the MLR potentials at the smallest [20 m s^{-1}, panels (a)] and largest [10^4 m s^{-1}, panels (d)] C_r considered, while at the intermediate C_r [10^3 m s^{-1}, panels (c)], the dependence of ϑ on b^2 is practically independent of the shape of the potential function. The range of b corresponding to quasi-orbiting collisions predicted by the LJ potential is shifted towards larger b compared to the MLR potential. Since the LJ potential usually overestimates the energy and force at repulsion, the values of ϑ calculated based on the LJ potential

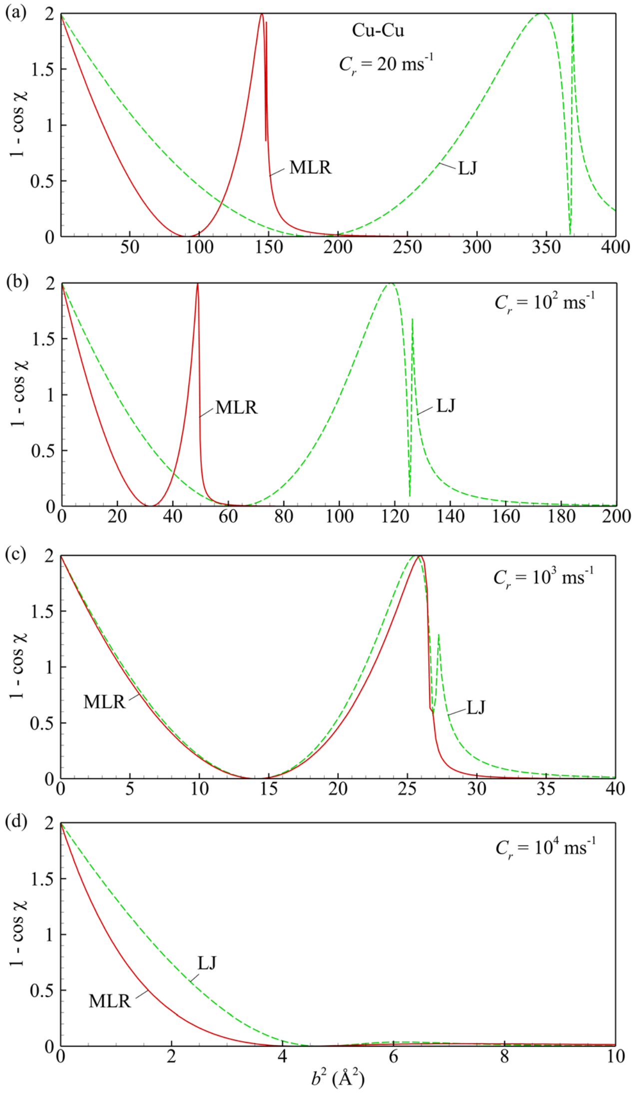

Fig. 5 Quantity $1 - \cos\chi$, where χ is the deflection angle defined by eqn (8), *versus* b^2 for two Cu atoms at a relative speed C_r of 20 m s^{-1} (a), 10^2 m s^{-1} (b), 10^3 ms^{-1} (c), and 10^4 ms^{-1} (d) calculated based on the MLR (red solid curves) and LJ (green dashed curves) potentials.

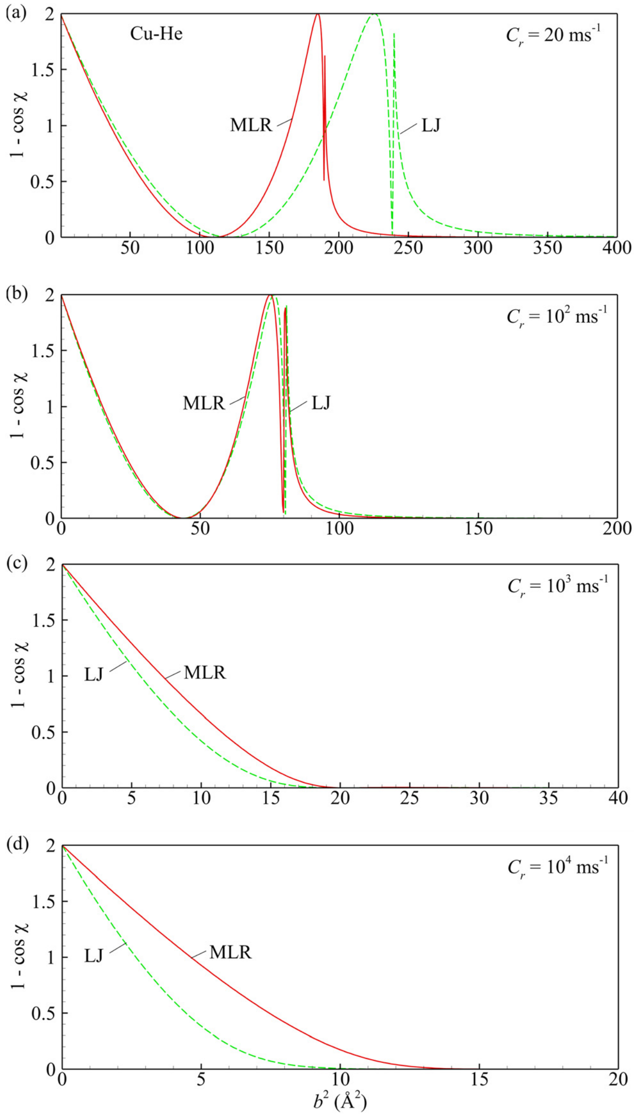

Fig. 6 Quantity $1 - \cos\chi$, where χ is the deflection angle defined by eqn (8), *versus* b^2 for a pair of Cu and He atoms at a relative speed C_r of 20 ms^{-1} (a), 10^2 ms^{-1} (b), 10^3 ms^{-1} (c), and 10^4 ms^{-1} (d) calculated based on the MLR (red solid curves) and LJ (green dashed curves) potentials.

for oblique collisions are greater than the values predicted based on the MLR potential for all atom pairs and C_r considered at small and large C_r. The only exclusion from this rule is provided by the Cu–He atom pair at large C_r [Fig. 6(c) and (d)]. It occurs since, for the Cu–He dimer, the LJ potential strongly underestimates the potential energy at repulsion [Fig. 2(b)].

For Ar–Ar collisions, the scattering matrices were additionally calculated based on the potential functions suggested in ref. 45, 50 and 51 (Fig. 4). The shape of the potential function has the most pronounced effect on the deflection angle at small and large C_r. At small C_r [Fig. 4(a)], the differences in the distributions of ϑ appear due to different asymptotic behavior of the potential functions at $r \to \infty$. The MLR potential predicts the smallest values of ϑ for nearly head-on collisions among all potentials considered, while the values of ϑ calculated based on the potential functions from ref. 45 and 50 practically coincide with each other at small and moderate speeds. At large C_r [Fig. 4(d)], the results obtained with different potential functions deviate from each other since the fitting coefficients in these functions do not allow to fit accurately the energy at $r \ll r_e$,[51] and the quality of the approximation fast deteriorates with reducing r at repulsion. The values of ϑ calculated based on the MLR potential practically coincide with the values based on the potential function of ref. 45. At intermediate C_r [Fig. 4(c)], the values of ϑ calculated based on different potential functions are close to each other.

A similar study of the effect of the PEC shape on the deflection angle is performed for collisions in the He–He and Xe–Xe atom pairs.[85] This study shows that the values of ϑ predicted based on the MLR potentials and potential functions developed in ref. 44 (for He–He) and ref. 48 (for Xe–Xe) practically coincide with each other at $C_r \geq 100\ \mathrm{m\ s^{-1}}$. This conclusion confirms a good agreement between the He–He PECs obtained in the QMC and CCSD(T) calculations. The disagreement between the asymptotic behaviors of different potential functions and, correspondingly, values of the deflection angle at $C_r \leq 100\ \mathrm{m\ s^{-1}}$, affects the predicted values of the transport coefficients of noble gases only at $T \ll 100$ K.[85] Thus, this disagreement is not relevant to the case of high-temperature gas mixtures considered in the present work.

4. Calculation of transport coefficients

4.1. Transport properties of binary mixtures

The obtained solutions of the classical scattering problem in the form of dependencies $\chi = \chi(b,C_r)$ are used to calculate the transport coefficients based on the Chapman–Enskog method in the form of the Sonine polynomial expansions.[23–31] For pure substances, the self-diffusivity $\mathfrak{D}$, shear viscosity μ, and thermal conductivity κ are calculated as functions of the gas temperature T. For binary gaseous mixtures, composed of Cu or Si vapor and a noble gas, the binary diffusivity $\mathfrak{D}$, shear viscosity μ, thermal conductivity κ, and thermal diffusion factor α_T are calculated as functions of temperature T and molar fraction of the noble gas x_g.

For pure substances and gas mixtures, the shear viscosity is defined in the same way as a coefficient that appears in the standard form of a Newtonian viscous tensor for monatomic gases.[23–25] The diffusion in a binary mixture, *i.e.*, the local difference between bulk velocities $\mathbf{u}_1$ and $\mathbf{u}_2$ of species 1 and 2, is described by the generalized Maxwell–Stefan law

$$\mathbf{u}_1 - \mathbf{u}_2 = -\mathfrak{D}\left[\frac{\nabla x_1}{x_1(1-x_1)} + \alpha_T \nabla \log T\right], \tag{10}$$

where x_1 is the molar fraction of species 1. In the present work, species 1 is always assumed to be a vapor and species 2 is assumed to be a noble gas. The chemical composition in such a mixture is described by the molar fraction of the noble gas $x_g = x_2$ so that eqn (10) can be re-written as

$$\mathbf{u}_\mathrm{v} - \mathbf{u}_\mathrm{g} = \mathfrak{D}\left[\frac{\nabla x_\mathrm{g}}{x_\mathrm{g}(1-x_\mathrm{g})} - \alpha_T \nabla \log T\right], \tag{11}$$

where $\mathbf{u}_\mathrm{v}$ and $\mathbf{u}_\mathrm{g}$ are the bulk velocities of the vapor and gas, respectively. When both species are at rest ($\mathbf{u}_\mathrm{v} = \mathbf{u}_\mathrm{g}$), a stationary chemical composition distribution is established in a non-isothermal mixture given as

$$\nabla x_\mathrm{g} = x_\mathrm{g}(1 - x_\mathrm{g})\alpha_T \nabla \log T. \tag{12}$$

The thermal diffusion leads to two kinds of thermal conductivities for gas mixtures: Partial κ' and steady-state κ thermal conductivity coefficients.[25] The quantity κ' characterizes conduction heat transfer in a mixture with a uniform chemical composition. The coefficient κ corresponds to the state when a time-independent chemical composition is established according to eqn (12). Henceforward, the steady state thermal conductivity κ is considered. It defines the heat flux $\mathbf{q}$ in the form[25]

$$\mathbf{q} = -\kappa\nabla T + nk_\mathrm{B}Tx_\mathrm{g}(1 - x_\mathrm{g})\alpha_T(\mathbf{u}_\mathrm{v} - \mathbf{u}_\mathrm{g}). \tag{13}$$

The calculation of the transport coefficients using the Sonine polynomial expansions is described in detail in ref. 96. In the present work, the expressions for the transport coefficient are used in the form obtained in ref. 53 and 54 in terms of the transport collision Ω-integrals

$$\Omega^{(l,s)}(T) = \sqrt{\frac{k_\mathrm{B}T}{2\pi m}}\int_0^\infty \exp\left(-\xi^2\right)\xi^{2s+3}Q^{(l)}\left(\sqrt{\frac{2k_\mathrm{B}T}{m}}\xi\right)\mathrm{d}\xi, \tag{14}$$

where

$$Q^{(l)}(C_r) = 2\pi\int_0^\infty \left[1 - \cos^l \chi(C_r, b)\right] b\,\mathrm{d}b \tag{15}$$

is the collision cross section and k_B is the Boltzmann constant, so that only a summary of these expressions is given below.

The diffusivity $\mathfrak{D}$, viscosity μ, thermal conductivity κ, and thermal diffusion factor α_T of a binary mixture are calculated as

$$\mathfrak{D} = \frac{3}{2}\frac{(1 - x_\mathrm{g})x_\mathrm{g}k_\mathrm{B}Td_0}{n(m_\mathrm{v} + m_\mathrm{g})} \tag{16}$$

$$\mu = \frac{5}{2}k_\mathrm{B}T\left[(1 - x_\mathrm{g})b_1 + x_\mathrm{g}b_{-1}\right], \tag{17}$$

$$\kappa = \frac{75}{8}{k_\mathrm{B}}^2T\left[\frac{(1 - x_\mathrm{g})a_1}{\sqrt{m_\mathrm{v}}} + \frac{x_\mathrm{g}a_{-1}}{\sqrt{m_\mathrm{g}}}\right], \tag{18}$$

$$\alpha_T = -\frac{5}{2}\frac{\sqrt{m_\mathrm{v} + m_\mathrm{g}}}{d_0}\left[\frac{d_1}{x_\mathrm{g}\sqrt{m_\mathrm{v}}} + \frac{d_{-1}}{(1 - x_\mathrm{g})\sqrt{m_\mathrm{g}}}\right], \tag{19}$$

where m_v and m_g are masses of vapor and noble gas atoms, respectively, and the coefficients b_1, b_{-1}, a_1, a_{-1}, d_1, d_0, and d_{-1} are determined by systems of linear algebraic equations. The details of calculations of these coefficients, which depend, in particular, on the adopted number of terms N in the expansions of the solution of the Boltzmann equation with respect to the Sonine polynomials, are provided in ref. 53.

To simplify notation, the subscripts that are often used for individual quantities in eqn (14)–(19) to denote participating atomic species are dropped. The atomic species define the value of the reduced mass m in eqn (14) and the potential function used to calculate the deflection angle in eqn (15). This simplified notation does not introduce any ambiguity in the presentation of results since the further discussion of all calculations based on eqn (14)–(19) is accompanied by explicit specification of species under consideration.

The viscosity and thermal conductivity of pure substances can be obtained from eqn (17) and (18) at $x_g = 0$ or $x_g = 1$. In this case, the coefficient $\mathfrak{D}$ becomes the gas self-diffusivity according to the definition adopted, *e.g.*, in ref. 2, if one uses eqn (16) at $x_g = x_v = 1/2$ and $m_g = m_v$.

The values of $\mathfrak{D}$, μ, and κ can be represented in a reduced form of Schmidt, Sc, and Prandtl, Pr, numbers

$$\mathrm{Sc} = \frac{\mu}{\rho\mathfrak{D}}, \tag{20}$$

$$\mathrm{Pr} = \frac{c_{\mathrm{p}}\mu}{\kappa}, \tag{21}$$

where $\rho = nm_x$ and $c_{\mathrm{p}} = (5/2)k_{\mathrm{B}}/m_x$ are the mass density and mean isobaric specific heat of the gas mixture, n is the total number density, and $m_x = m_{\mathrm{v}}(1 - x_{\mathrm{g}}) + m_{\mathrm{g}}x_{\mathrm{g}}$ is the average atom mass. The Schmidt and Prandtl numbers can be used to characterize the difference in the variation of $\mathfrak{D}$ and κ with temperature with respect to μ.

4.2. Numerical calculation of the Ω-integrals and transport coefficients

The transport collision integrals and transport coefficients are calculated in the range of temperature from 10 K to 10^4 K, however, the transport coefficients for Cu and Si vapors and their mixtures with noble gases are further discussed only at $T \geq 100$ K. At smaller temperatures, the values of the transport coefficients can be sensitive to the peculiarities of the asymptotic behavior of the potential functions at $r \to \infty$. The low-temperature gas properties, however, are out of the scope of the present paper.

The integrals in eqn (14) and (15) are calculated numerically using the preliminarily determined scattering matrices $\chi_{ij} = \chi(C_{ri},b_j)$, so that the numerical accuracy of calculations of the Ω-integrals implicitly depends on the accuracy of numerical calculation of individual deflection angles according to eqn (8). The numerical accuracy of calculations of the Ω-integrals also depends on the integration step sizes Δb and ΔC_r used for numerical quadrature as well as on the cutoff values of the impact parameter b_* and relative speed C_{r*} that replace the top integration limits in the improper integrals of eqn (14) and (15). The accuracy of the transport coefficients also depends on the number of terms N in the Sonine polynomial expansions.

In the present work, two independently developed codes for calculations of the deflection angle and Ω-integrals were used. The codes use different approaches for numerical quadrature in eqn (8), but the maximum relative difference between $\vartheta = 1 - \cos\chi$ predicted by both codes does not exceed 10^{-6} with exception of sliding collisions at large b, which do not contribute to the Ω-integrals. The first code is based on the numerical quadrature of eqn (14) and (15) on meshes with equal spacings Δb and ΔC_r. The second code utilizes non-homogeneous meshes for both b and C_r.

The comprehensive convergence studies were performed for both codes. Based on the results of this study, the values of $b_* = 20$ Å, $\Delta b = 0.005$ Å, and $\Delta C_r = 2.5\ \mathrm{m\ s^{-1}}$ are chosen for numerical integration in eqn (14) and (15) with the first code, while the value of C_{r*} is chosen individually for different atom pairs.[85] In this case, the direct calculations showed that the estimated error in the value of all transport coefficients for pure substances does not exceed 0.04%. The numerical accuracy of the second code was investigated in ref. 30, 53, and 54. For the second code, the estimated relative error in the values of the transport coefficients does not exceed 0.01% for both pure substances and gaseous mixtures.

In the present work, the calculations are performed with N = 1, 2, and 10. The results that are further presented and discussed in Sections 5 and 6, however, are all obtained with N = 10 with exception of Table 4, where the results are calculated with N = 1 and N = 2.

4.3. Transport coefficients in the first approximation with respect to the Sonine polynomial expansions

It is instructive to use the one-term expansions of the transport coefficients. Such one-term expansions are simple and can be easily presented in an algebraic form. These one-term expansions are also usually used for the fitting of the HS, VHS, and VSS molecular models.[22]

At $N = 1$, eqn (16) for $x_{\mathrm{g}} = 1/2$ and $m_{\mathrm{g}} = m_{\mathrm{v}}$ reduces to

$$\mathfrak{D} = \frac{3}{8}\frac{k_{\mathrm{B}}T}{\Omega^{(1,1)}(T)}\frac{1}{2mn}, \tag{22}$$

while eqn (17) and (18) for $x_{\mathrm{g}} = 0$ or $x_{\mathrm{g}} = 1$ reduce to

$$\mu = \frac{5}{8}\frac{k_{\mathrm{B}}T}{\Omega^{(2,2)}(T)}, \tag{23}$$

$$\kappa = \frac{15}{16}\frac{k_{\mathrm{B}}T}{\Omega^{(2,2)}(T)}\bar{c}_{\mathrm{p}}, \tag{24}$$

where $\bar{c}_{\mathrm{p}} = (5/2)k_{\mathrm{B}}/(2m)$. Eqn (22)–(24) represent the one-term (first) approximations of the self-diffusivity, viscosity, and thermal conductivity of pure substances with respect to the Sonine polynomial expansions. These equations also define the "contributions" of collisions between corresponding atom pairs to the one-term approximations of binary diffusivity, viscosity, and thermal conductivity of gaseous mixtures.[24]

For pure substances, the second terms in the Sonine polynomial expansions provide corrections to the first-order approximations not greater than 0.8% for all cases considered in the present work at temperatures between 10^2 K and 10^4 K (Table 4). The total contributions of further terms from third to tenth are found to be less than 0.1%.

In the first approximation, for a gas mixture composed of species 1 and 2, the binary diffusivity is defined by eqn (22), while the viscosity, thermal conductivity, and thermal diffusion factor are determined algebraically by complex equations[24] that can be represented in the form

$$\mu = \mu_{12}f_{\mu}\left(m_1, m_2, \frac{\mu_1}{\mu_{12}}, \frac{\mu_2}{\mu_{12}}, \frac{\Omega_{12}^{(1,2)}}{\Omega_{12}^{(1,1)}}, \frac{\Omega_{12}^{(1,3)}}{\Omega_{12}^{(1,1)}}, \frac{\Omega_{12}^{(2,2)}}{\Omega_{12}^{(1,1)}}, x_2\right), \tag{25}$$

$$\kappa = \kappa_{12}f_{\kappa}\left(m_1, m_2, \frac{\kappa_1}{\kappa_{12}}, \frac{\kappa_2}{k_{12}}, \frac{\Omega_{12}^{(1,2)}}{\Omega_{12}^{(1,1)}}, \frac{\Omega_{12}^{(1,3)}}{\Omega_{12}^{(1,1)}}, \frac{\Omega_{12}^{(2,2)}}{\Omega_{12}^{(1,1)}}, x_2\right), \tag{26}$$

$$\alpha_T = f_{\alpha}\left(m_1, m_2, \frac{\kappa_1}{\kappa_{12}}, \frac{\kappa_2}{k_{12}}, \frac{\Omega_{12}^{(1,2)}}{\Omega_{12}^{(1,1)}}, \frac{\Omega_{12}^{(1,3)}}{\Omega_{12}^{(1,1)}}, \frac{\Omega_{12}^{(2,2)}}{\Omega_{12}^{(1,1)}}, x_2\right), \tag{27}$$

where μ_k and κ_k are the viscosity and thermal conductivity of pure substance k calculated based on eqn (23) and (24), while μ_{12} and κ_{12} are quantities that are calculated based on the same eqn (23) and (24) but using the reduced mass m and Ω-integrals for cross-species collisions $\Omega_{12}^{(1,s)}(T)$. These equations show that the viscosity and thermal conductivity of a gas mixture to

Table 4 Difference $\Delta[\mu] = 100\% \times (\mu - \mu_{\mathrm{PF}})/\mu$ between viscosities μ of pure substances calculated based on the MLR potentials with the two-terms expansions of the transport coefficients ($N = 2$) and viscosities μ_{PF} found based on other potential functions (PF) or with the one-term expansions ($N = 1$) at various temperatures T. $\Delta[\mu]_{\mathrm{A}}$ is the RMS value of $\Delta[\mu]$ in the range of temperature from 10^2 K to 10^4 K

			T (K)						
PF	N	$\Delta[\mu]_{\mathrm{A}}$	100	200	300	1000	2000	3000	10 000
Helium gas									
MLR	1	0.298	0.650	0.664	0.643	0.516	0.397	0.312	0.0628
LJ	2	24.4	3.07	4.67	5.86	10.9	15.4	19.0	33.7
Ref. 50	2	11.9	3.06	3.77	4.18	5.63	7.22	8.77	17.0
Ref. 44	2	0.914	0.477	0.376	0.194	0.860	1.35	1.27	1.44
Ref. 51	2	2.61	1.18	1.31	1.28	0.832	0.765	1.11	4.40
Argon gas									
MLR	1	0.592	0.00511	0.0324	0.290	0.623	0.673	0.658	0.530
LJ	2	9.05	3.21	1.10	0.851	1.85	3.16	4.20	8.97
Ref. 50	2	4.70	0.753	0.379	0.978	2.46	3.36	3.95	6.25
Ref. 45	2	0.286	0.733	0.209	0.0112	0.210	0.168	0.0709	0.523
Ref. 51	2	0.124	0.243	0.0949	0.0686	0.113	0.159	0.155	0.111
Xenon gas									
MLR	1	0.573	0.178	0.00753	0.00876	0.407	0.609	0.641	0.551
LJ	2	5.11	8.98	4.28	2.35	1.25	2.22	3.15	7.77
Ref. 50	2	3.80	0.674	0.950	1.09	1.59	2.28	2.85	5.741
Ref. 48	2	0.219	0.0759	0.130	0.133	0.165	0.205	0.223	0.231
Ref. 51	2	1.64	3.41	1.67	0.965	0.519	0.802	1.07	2.42
Cu vapor									
MLR	1	0.518	0.566	0.595	0.605	0.586	0.579	0.701	0.583
LJ	2	17.2	32.9	26.2	21.8	7.23	1.93	8.26	19.6
Si vapor									
MLR	1	0.214	0.204	0.213	0.218	0.232	0.235	0.232	0.0929
LJ	2	6.88	1.28	0.198	0.553	3.22	5.01	6.14	7.58

a large extent depend on the "contributions" μ_{12} and κ_{12} of cross-species collisions. The binary diffusion coefficient in the second approximation is determined by an equation similar to eqn (25), which will include the self-diffusivity $\mathfrak{D}_k$ and binary diffusivity $\mathfrak{D}_{12}$ calculated in the first approximation based on eqn (22).[24] For a binary mixture with arbitrary chemical composition, the contributions of the second and further terms in the Sonine polynomial expansions, as a rule, are larger than for the corresponding pure substances.

4.4. Effect of the PEC shape on the values of the Ω-integrals

According to eqn (22)–(24), the effect of temperature on the transport coefficients of pure substances is dominated by integrals $\Omega^{(1,1)}(T)$ and $\Omega^{(2,2)}(T)$. Eqn (25)–(27) show that the corresponding integrals for cross-species collisions also determine (together with $\Omega^{(1,2)}_{12}$ and $\Omega^{(1,3)}_{12}$) the first-order coefficients of gas mixtures.

For collision pairs involving a Cu atom, the effect of the PEC shape on the dependences of $\Omega^{(1,1)}$ and $\Omega^{(2,2)}$ on temperature is illustrated in Fig. 7. The plots in this figure are obtained based on the MLR and LJ potentials with the parameters from Table 3, and the results are presented in the form of the reduced Ω-integrals

$$\Omega^{(l,s)*}(T) = \frac{\Omega^{(l,s)}(T)}{\Omega^{(l,s)}_{\mathrm{HS}}(T)}, \tag{28}$$

where

$$\Omega^{(l,s)}_{\mathrm{HS}}(T) = C^{(l,s)}\pi\sigma^2\sqrt{\frac{k_{\mathrm{B}}T}{2\pi m}} \tag{29}$$

is a corresponding integral for HS particles of diameter σ and

$$C^{(l,s)} = \frac{(s+1)!}{2}\left[1 - \frac{1}{2}\frac{1+(-1)^l}{1+l}\right], \tag{30}$$

as functions of the reduced temperature $T^* = k_{\mathrm{B}}T/D_{\mathrm{e}}$. Following the approach adopted in ref. 24, where σ corresponds to the zero-energy distance of the LJ potential, the length scale σ in eqn (29) is used in the form $\sigma = r_{\mathrm{e}}/\sqrt[6]{2}$. The calculated values of $\Omega^{(1,1)*}$ and $\Omega^{(2,2)*}$ for other collision pairs are presented in the ESI.† In all cases, the calculations are performed for a temperature range from 10 K to 10^4 K.

All these calculations result in consistent conclusions regarding the effect of the PEC shape. In general, in the logarithmic scale, the plots of the Ω-integrals include three quasi-linear parts, where the integrals roughly follow the power scaling laws with temperature, at $T^* \lesssim 0.2$, $0.2 \lesssim T^* \lesssim 2$, and $T^* \gtrsim 2$. This is realized, *e.g.*, in the Cu–Ar case [Fig. 7(c)]. For other atom pairs, due to the strong variability of D_{e}, the range of temperature, $10\ \mathrm{K} \leq T \leq 10^4$ K, may not contain all three characteristic sub-ranges of T^*. The values of the Ω-integrals calculated based on the MLR and LJ potentials usually agree with each other reasonably well in the mid-range $0.2 \lesssim T^* \lesssim 2$. The degree of disagreement between the MLR- and LJ-based

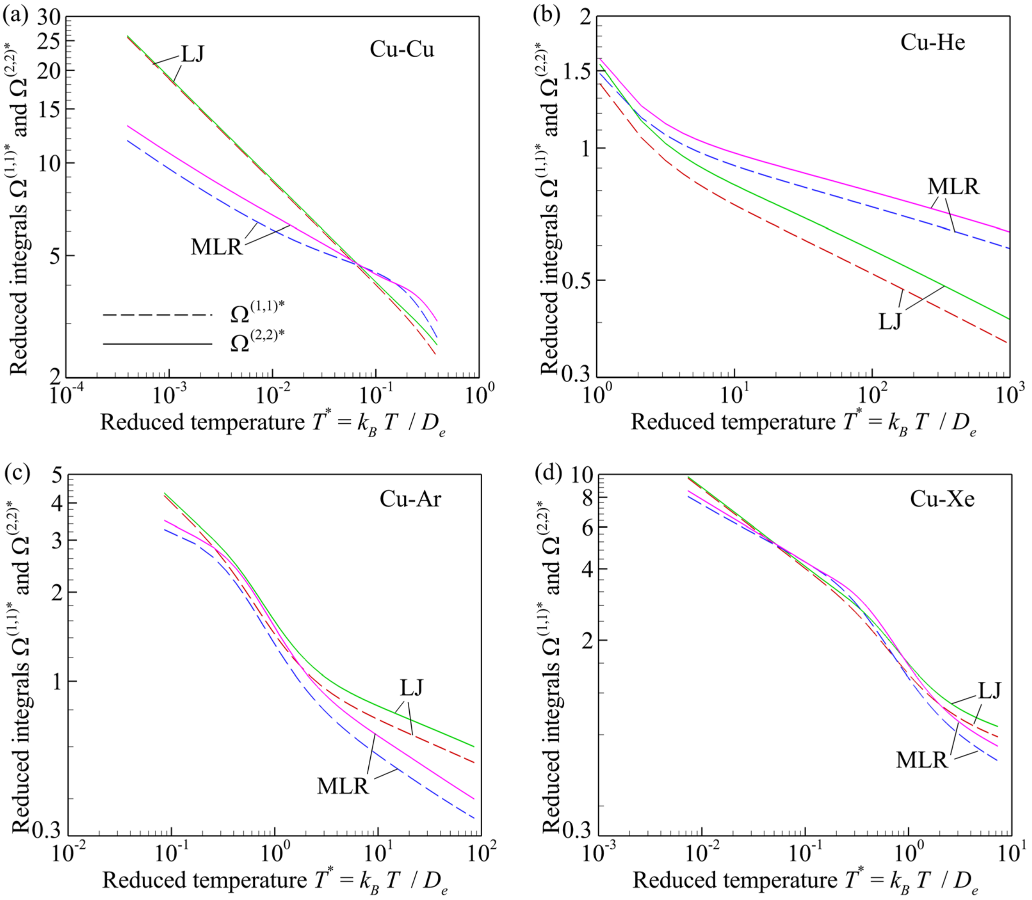

Fig. 7 Reduced integrals $\Omega^{(1,1)\star}$ (dashed curves) and $\Omega^{(2,2)\star}$ (solid curves) for the Cu–Cu (a), Cu–He (b), Cu–Ar (c), and Cu–Xe (c) atom pairs *versus* reduced temperature $T^\star = k_\mathrm{B}T/D_\mathrm{e}$ calculated based on the LJ (red and green curves) and MLR (blue and magenta curves) potentials. The scale $\sigma = r_\mathrm{e}/\sqrt[6]{2}$ is used in eqn (29).

values of the Ω-integrals grows fast with both an increase and decrease in $T^\star$ outside this range. The maximum disagreement is observed for the Cu–Cu and He–He pairs. In V–G atom pairs, where V is a Cu or Si atom and G is a noble gas atom, the maximum disagreement between the Ω-integrals calculated based on the MLR and LJ potentials is observed in pairs containing He atoms. This disagreement decreases with an increasing mass of the noble gas atoms.

5. Transport properties of pure substances

5.1. Noble gases

For helium, argon, and xenon gases, the transport coefficients calculated based on the *ab initio* PECs are well-known.[30,52,57] In the present work, therefore, the transport coefficients of noble gases are calculated to validate the numerical approach and reveal the effect of the PEC shape.

For argon and xenon, the viscosities predicted based on the MLR and LJ potentials closely agree at $T^\star \sim 1$. For helium, the difference in viscosities calculated based on the MLR and LJ potentials remains relatively large in the whole temperature range considered. The average differences $\Delta[\mu]_\mathrm{A}$ between the MLR- and LJ-based viscosities are ${\sim}24\%$, ${\sim}9\%$, and 5% for He, Ar, and Xe gases, respectively (Table 4). The viscosity calculated based on the MLR potentials agrees well with the viscosity calculated based on the potential functions established in the CCSD(T) calculations in ref. 44 for He (average disagreement $\Delta[\mu]_\mathrm{A} \sim 1\%$), ref. 45 for Ar ($\Delta[\mu]_\mathrm{A} \sim 0.3\%$), and ref. 48 for Xe ($\Delta[\mu]_\mathrm{A} \sim 0.3\%$) (Table 4). The universal potential function for the noble gas dimers developed in ref. 51 provides the viscosity data that agree well with the MLR potential for Ar ($\Delta[\mu]_\mathrm{A} \sim 0.1\%$) but demonstrate worse agreement for He and Xe. The viscosity obtained based on the potentials suggested in ref. 50 strongly deviates from the viscosity based on the MLR potential with the average differences that are only twice smaller than the corresponding differences for the LJ potential.[85]

5.2. Cu and Si vapors

For Cu and Si vapors, the selected values of diffusivity, viscosity, and thermal conductivity are given in the Appendix. The additional values of the transport coefficients are provided in the form of individual text files as a part of the ESI.† The viscosity of Cu vapor as a function of temperature shown in double logarithmic scale is non-linear with the slope strongly changing

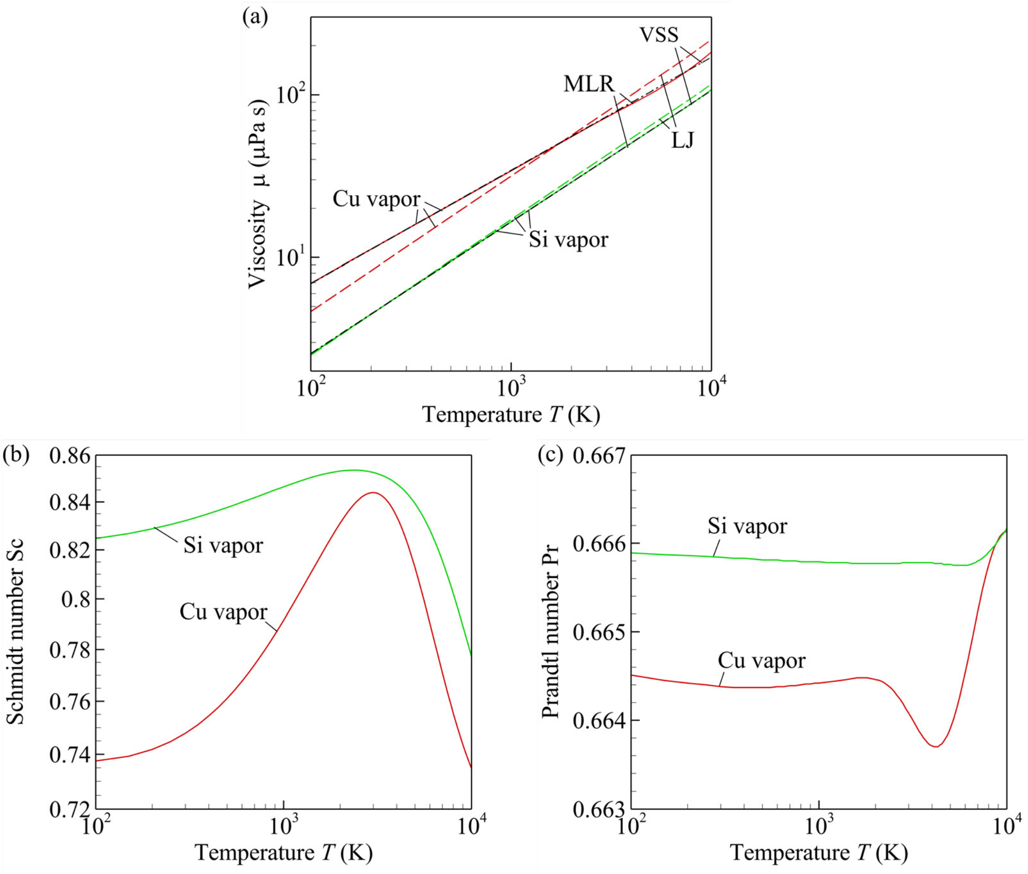

Fig. 8 Viscosity μ (a), Schmidt number Sc (b), and Prandtl number Pr (c) of copper (red solid curves) and silicon (green solid curves) vapors obtained based on the MLR potentials. In panel (a), the red and green dashed curves correspond to the viscosity of copper and silicon vapors, respectively, calculated based on the LJ potentials; the black dashed-dotted curves are obtained based on the VSS model for copper and silicon vapors with the parameterizations marked with "*" in Table 6. The solid and dashed-dotted curves for silicon vapor visually coincide with each other in panel (a).

at $T \sim 5000$ K [Fig. 8(a)]. This suggests that the viscosity cannot be accurately approximated by a power law in the whole range of temperature considered. The viscosity of Si vapor, on the contrary, demonstrates power scaling with temperature. The average differences $\Delta[\mu]_A$ between the MLR- and LJ-based viscosities are ~17% and ~7% for Cu and Si vapors, respectively (Table 4). This makes the LJ potential not suitable for high-fidelity calculations of the transport coefficients. It also means that the parametrizations of the LJ potential for Cu and Si vapors based on viscosity data or other indirect experimental measurements may not provide accurate values of D_e and r_e.

The difference in the scaling behavior of diffusivity and thermal conductivity with respect to viscosity can be characterized by the Schmidt and Prandtl numbers. For pure substances, using the one-term expansions with respect to the Sonine polynomials, eqn (20) and (21) reduce to

$$\mathrm{Sc} = \frac{10}{6}\frac{\Omega^{(1,1)}(T)}{\Omega^{(2,2)}(T)}, \tag{31}$$

$$\mathrm{Pr} = \frac{2}{3}. \tag{32}$$

It is well known that for noble gases both the Schmidt and Prandtl numbers are weak functions of temperature, *e.g.*, Sc varies between 0.71 and 0.78.[32] The computations for Cu and Si vapors reveal somewhat stronger but still weak variability of Sc and Pr with temperature [Fig. 8(b) and (c)], when Sc varies between ~0.73 and ~0.85, while Pr varies between ~0.6635 and ~0.6662. This indicates a similar scaling behavior of all transport coefficients of Cu and Si vapors with respect to T.

5.3. Cross-species collisional contributions

Fig. 9 shows the values of $\mathfrak{D}$ and μ calculated based on eqn (22) and (23) for cross-species collisions. These quantities partially describe the contributions of the cross-species collisions to the viscosity of binary mixtures in the form of the one-term expansion with respect to the Sonine polynomials according to eqn (25) and binary diffusivity in the second approximation. In agreement with the previous analysis of the Ω-integrals for the cross-species collisions, these results reveal a strong difference between the values of $\mathfrak{D}$ and μ calculated based on the MLR and LJ potentials for collisions involving He and Ar atoms. In the logarithmic scale, the temperature dependences of $\mathfrak{D}$ and μ are practically linear for collision pairs involving He atoms. The results of calculations of κ based on eqn (24) are not shown but

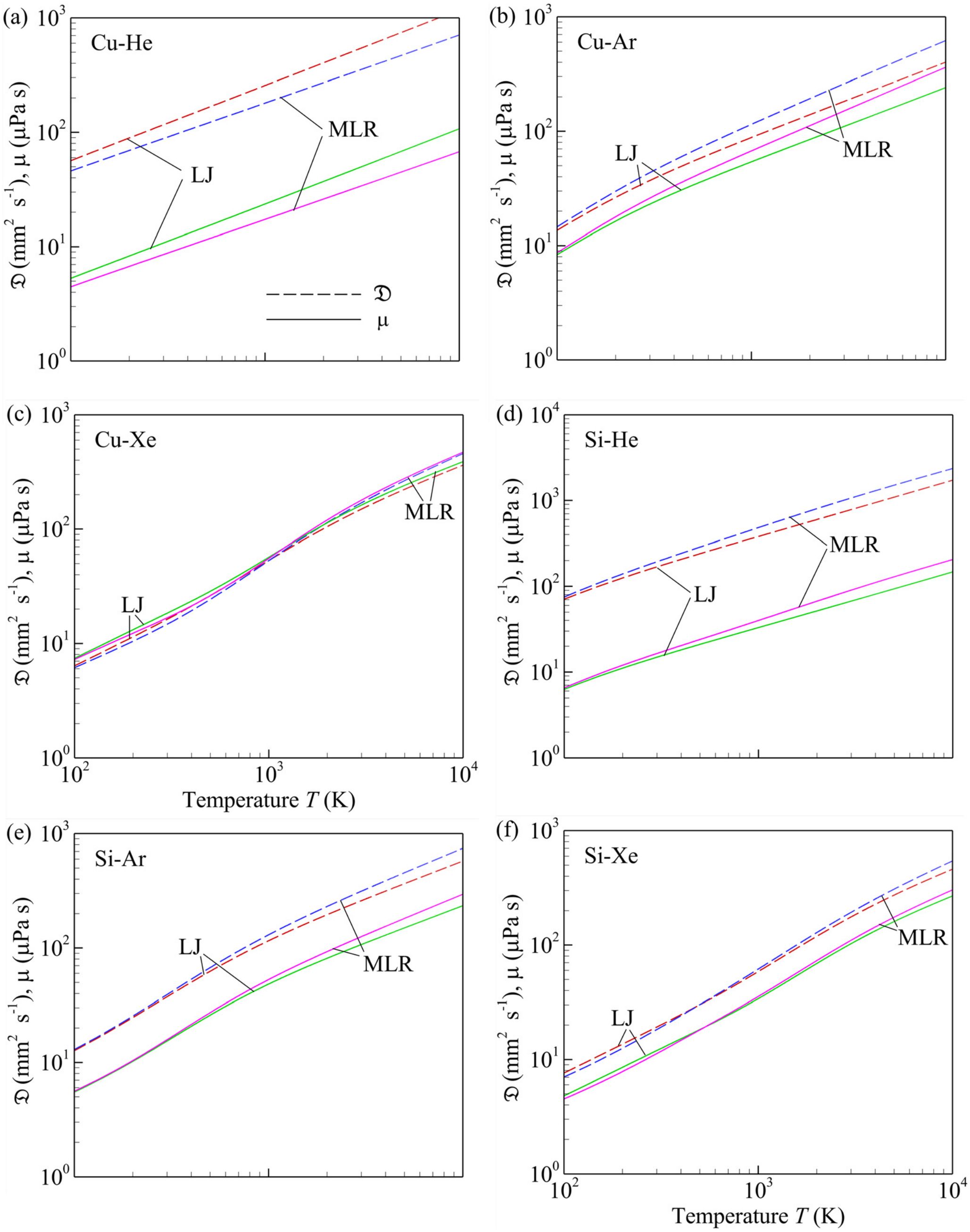

Fig. 9 Contributions to diffusivity $\mathfrak{D}$ [eqn (22) at a number density of $n = 10^{19}$ cm^{-3}, dashed curves] and viscosity μ ([eqn (23)], solid curves) in gas mixtures provided by collisions in the Cu–He (a), Cu–Ar (b), Cu–Xe (c), Si–He (d), Si–Ar (e), and Si–Xe (f) atom pairs *versus* temperature T calculated based on the LJ (red and green curves) and MLR (blue and magenta curves) potentials.

they demonstrate the same qualitative trends that can be observed for μ.

6. Transport properties of binary mixtures

The values of the transport coefficients of all binary mixtures, which are considered as functions of temperature T and gas molar fraction x_g, are provided in the ESI,† in the form of individual text files. In this section, only a selection of the obtained results is described.

6.1. Cu–He, Cu–Ar, and Cu–Xe mixtures

The values of the transport coefficients calculated for the Cu–He, Cu–Ar, and Cu–Xe binary mixtures based on the MLR potentials are shown as functions of the noble gas molar fraction x_g in Fig. 10. As expected, at constant pressure, the binary diffusivity $\mathfrak{D}$ only marginally changes depending on the chemical composition. It occurs since the binary diffusion is

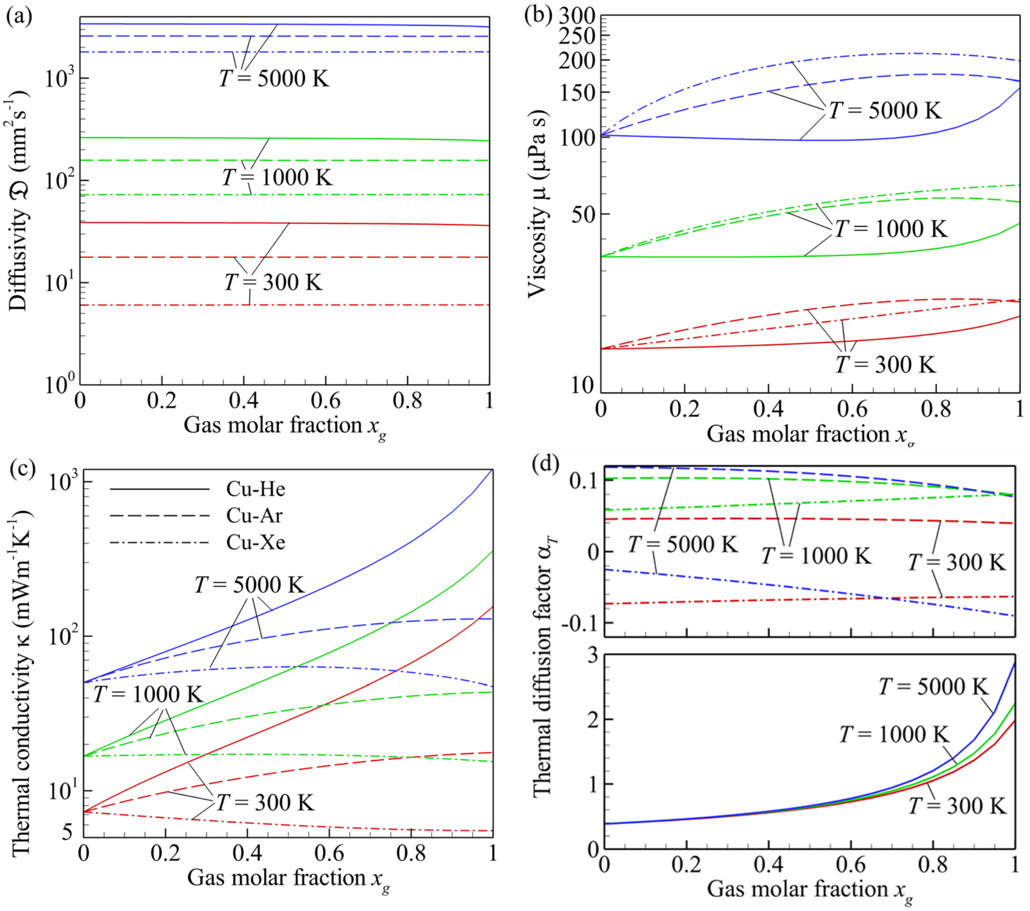

Fig. 10 Binary diffusivity 𝔇 (a), viscosity μ (b), thermal conductivity κ (c), and thermal diffusion factor α_T (d) of the Cu–He (solid curves), Cu–Ar (dashed curves), and Cu–Xe (dashed-dotted curves) mixtures *versus* molar fraction of noble gas x_g at a temperature of T = 300 K (red curves), 1000 K (green curves), and 5000 K (blue curves). The diffusivity is calculated at a pressure of 1 atm = 101 325 Pa. All calculations are performed based on the MLR potentials and ten-term expansions with respect to the Sonine polynomials.

dominated by the first term given by eqn (22), which does not depend on molar fractions, while the dependence on x_g appears only in the higher approximations with respect to the Sonine polynomials. The values of the binary mixture viscosity and thermal conductivity strongly depend on x_g as these dependencies appear already in the first approximation.[24]

For light-weight helium, the mixture viscosity is practically not affected by the presence of the noble gas and remains equal to the viscosity of Cu vapor up to x_g = 0.7. The thermal conductivity of the mixture, on the contrary, strongly varies even at small x_g. For the Cu–He mixture, the variability of κ with x_g is strongest among all mixtures considered in Fig. 10. It occurs since the thermal conductivity in the first approximation is inversely proportional to the reduced mass m [eqn (24)].

The variations of the transport coefficients with x_g in the mixtures of Cu vapor with heavier argon and xenon gases are qualitatively similar to each other. The transport coefficients of these mixtures demonstrate an abnormal behavior when the mixture viscosity and thermal conductivity can be larger than the coefficients of the corresponding pure substances. The viscosity of such mixtures can non-monotonically vary with x_g, when the maximum viscosity is achieved at $0.6 < x_g < 0.8$.

The thermal diffusion factor in the Cu–He mixture has large positive values at large molar fraction of He. According to eqn (11), the positive sign of α_T means that thermal diffusion promotes diffusion of vapor atoms into a cooler region, while the helium atoms move to a hotter region. Such a situation is characteristic in a mixing layer at the edge of a laser-induced vapor plume expanding into a background gas, *e.g.*, ref. 21. In the Cu–Ar mixture, α_T is also positive, while in the Cu–Xe mixture, the sign of α_T is negative at small and large temperatures.

Contrary to pure substances, where the Schmidt, Sc, and Prandtl, Pr, numbers are known to be conservative parameters, Sc and Pr of gas mixtures demonstrate much stronger variability as functions of temperature and molar fraction (Fig. 11). It is found that Sc can vary within two orders of magnitude in a mixture of heavy vapor and light noble gas, *e.g.*, the Cu–He mixture, due to the variation of mass density ρ in eqn (20). The modified Schmidt number

$$\overline{\mathrm{Sc}} = \frac{\mu}{\bar{\rho}\mathfrak{D}} = \mathrm{Sc}\frac{\rho}{\bar{\rho}}, \tag{33}$$

which is based on the mean density $\bar{\rho} = n(m_1 + m_2)/2$ that is independent of the chemical composition, is found to be a

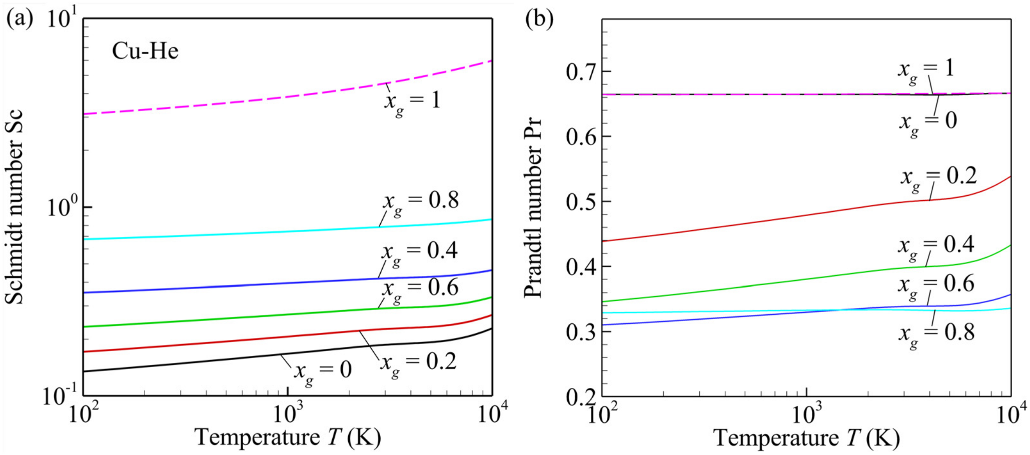

Fig. 11 Schmidt number Sc (a) and Prandtl number Pr (b) of the Cu–He mixture *versus* temperature T at a noble gas molar fraction of x_g = 0 (black curves), 0.2 (red curves), 0.4 (green curves), 0.6 (blue curves), 0.8 (cyan curves), and 1 (magenta dashed curves). All calculations are performed based on the MLR potentials and ten-term expansions with respect to the Sonine polynomials.

more conservative parameter. For the Cu–He gas mixture, both $\overline{\mathrm{Sc}}$ and Pr vary within the range from ∼0.3 to ∼0.7 in the whole temperature range under consideration.

6.2. Si–He, Si–Ar, and Si–Xe mixtures

The calculated transport coefficients of mixtures of Si vapor with noble gases are presented in Fig. 12. Qualitatively, the transport properties of these mixtures demonstrate the same trends as in the case of the corresponding Cu-noble gas mixtures. The only exclusion from this rule is the viscosity of the Si–He mixture, which almost linearly increases with the gas molar fraction up to $x_g \sim 0.9$ and then remains constant with further increase of x_g.

6.3. Effects of the PEC shape on the transport coefficients in binary mixtures

The ratios of the transport coefficients calculated based on the LJ and MLR potentials for the Cu–He mixture are presented in Fig. 13. As one can see, the differences between the results obtained with these two potentials can be as large as 50–60% for all transport coefficients. The differences tend to increase with increasing mixture temperature. It occurs because the LJ potential, as a rule, strongly overestimates the magnitude of interatomic forces at $r < r_e$. The differences between the transport coefficients for this gas mixture are larger than the typical differences between the transport coefficients predicted based on the MLR and LJ potential for pure substances (Table 4).

The calculations of the transport coefficients based on the LJ potentials for other gas mixtures reveal the same trends and similar levels of discrepancy with respect to the values predicted based on the MLR potentials. For instance, the calculations for the Cu–Ar mixture reveal the maximum discrepancies of ∼35% between the MLR- and LJ-based binary diffusivities $\mathfrak{D}$, viscosities μ, and thermal conductivities κ, while the thermal diffusion factor α_T calculated based on the LJ potential can be, depending on temperature, twice smaller or larger than α_T calculated based on the MLR potentials.[85] These results confirm that the LJ potentials may not be a good PEC approximation for high-fidelity calculations of the transport of properties of gas mixtures composed of such dissimilar components as Cu or Si vapor and a noble gas.

7. Parameters of molecular models for kinetic simulations of gas flows

7.1. Variable hard sphere (VHS) model

In the VHS molecular model,[22,26] the gas molecules are considered as hard spheres with isotropic scattering at binary collisions and variable diameter which is defined as

$$d_{\mathrm{VHS}} = d_{\mathrm{VHS,ref}}\left(\frac{C_{r,\mathrm{ref}}}{C_r}\right)^{\omega-1/2}, \qquad (34)$$

where

$$C_{r,\mathrm{ref}} = \frac{\sqrt{2k_{\mathrm{B}}T_{\mathrm{ref}}/m}}{\Gamma^{1/(2\omega-1)}(5/2-\omega)} \qquad (35)$$

is the reference relative velocity, $\Gamma(x)$ is the gamma function, $d_{\mathrm{VHS,ref}}$ is the reference diameter at a reference temperature T_{ref}, and ω is the viscosity index. The parameters $d_{\mathrm{VHS,ref}}$ and ω of the VHS model are usually determined by fitting the gas viscosity data.[22]

In the VHS model, the deflection angle is equal to

$$\chi(C_r, b) = 2\arccos\left(\frac{b}{d_{\mathrm{VHS}}(C_r)}\right). \qquad (36)$$

By using eqn (36) in eqn (15), one can obtain, in the first approximation with respect to the Sonine polynomials, power laws for self-diffusivity, viscosity, and thermal conductivity of a pure substance:

$$\mathfrak{D}_{\mathrm{VHS}} = \mathfrak{D}_{\mathrm{VHS,ref}}\frac{n_{\mathrm{ref}}}{n}\left(\frac{T}{T_{\mathrm{ref}}}\right)^{\omega}, \qquad (37)$$

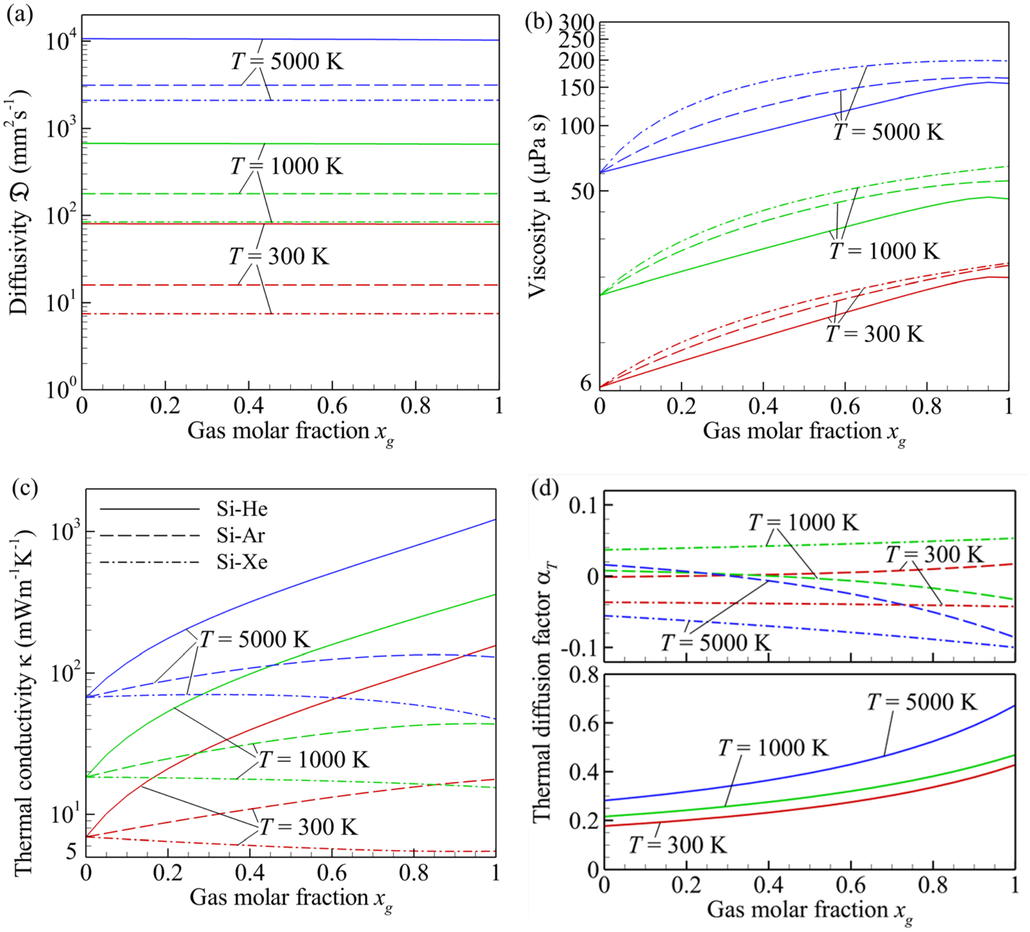

Fig. 12 Binary diffusivity $\mathfrak{D}$ (a), viscosity μ (b), thermal conductivity κ (c), and thermal diffusion factor α_T (d) of the Si–He (solid curves), Si–Ar (dashed curves), and Si–Xe (dashed-dotted curves) mixtures *versus* molar fraction of noble gas x_g at a temperature of T = 300 K (red curves), 1000 K (green curves), and 5000 K (blue curves). The diffusivity is calculated at a pressure of 1 atm. All calculations are performed based on the MLR potentials and ten-term expansions with respect to the Sonine polynomials.

$$\mu_{\mathrm{VHS}} = \mu_{\mathrm{VHS,ref}}\left(\frac{T}{T_{\mathrm{ref}}}\right)^{\omega}, \tag{38}$$

$$\kappa_{\mathrm{VHS}} = \kappa_{\mathrm{VHS,ref}}\left(\frac{T}{T_{\mathrm{ref}}}\right)^{\omega}, \tag{39}$$

where n_{ref} is the reference number density, and the reference values of the transport coefficients at a reference temperature T_{ref} are equal to

$$\mathfrak{D}_{\mathrm{VHS,ref}} = \frac{3\sqrt{\pi}}{8\Gamma(7/2-\omega)\pi d_{\mathrm{VHS,ref}}{}^2 n_{\mathrm{ref}} C_{r,\mathrm{ref}}^{2\omega-1}}\left(\frac{2k_{\mathrm{B}}T_{\mathrm{ref}}}{m}\right)^{\omega}, \tag{40}$$

$$\mu_{\mathrm{VHS,ref}} = \frac{15m}{(5-2\omega)(7-2\omega)d_{\mathrm{VHS,ref}}{}^2}\sqrt{\frac{k_{\mathrm{B}}T_{\mathrm{ref}}}{2\pi m}}, \tag{41}$$

$$\kappa_{\mathrm{VHS,ref}} = \frac{\bar{c}_{\mathrm{p}}\mu_{\mathrm{VHS,ref}}}{\overline{\mathrm{Pr}}}, \tag{42}$$

where $\overline{\mathrm{Pr}} = 2/3$

For binary mixtures, the transport coefficients in the form of the one-term expansions with respect to the Sonine polynomials are defined by eqn (22) and (25)–(27). All Ω-integrals for the VHS (and VSS) molecular model vary with temperature as $\Omega^{(l,s)} \propto T^{1-\omega}$, so that the fractions $\Omega^{(l,s)}/\Omega^{(1,1)}$ in eqn (25)–(27) are independent of temperature. Then the temperature dependences of the transport coefficients of a mixture are determined by the dependences of the coefficients of the corresponding pure substances, *e.g.*, μ_1 and μ_2, and contributions of the cross-species collisions, *e.g.*, μ_{12}. This means that the parameters of the VHS (and VSS) model for cross-species collisions, $d_{\mathrm{VHS,12}}$ and ω_{12}, must be determined to fit the temperature dependence of μ_{12} (and $\mathfrak{D}_{12}$ for the VSS model, Section 7.2) using the same approach, which is used to fit the model parameters for collisions between particles of the same chemical sort.

The actual dependence of viscosity on temperature is not described by the power law in eqn (38), and, thus, the parameters of the model, $d_{\mathrm{VHS,ref}}$ and ω, depend on the choice of the range of temperature or a single temperature value, where the viscosity data are used to parameterize the model. The values of $d_{\mathrm{VHS,ref}}$ and ω can be found to fit exactly the values of μ and $\mathrm{d}\mu/\mathrm{d}T$ at some temperature T_{ref}. Here, we use another approach, where the viscosity exponent ω is first derived from the least

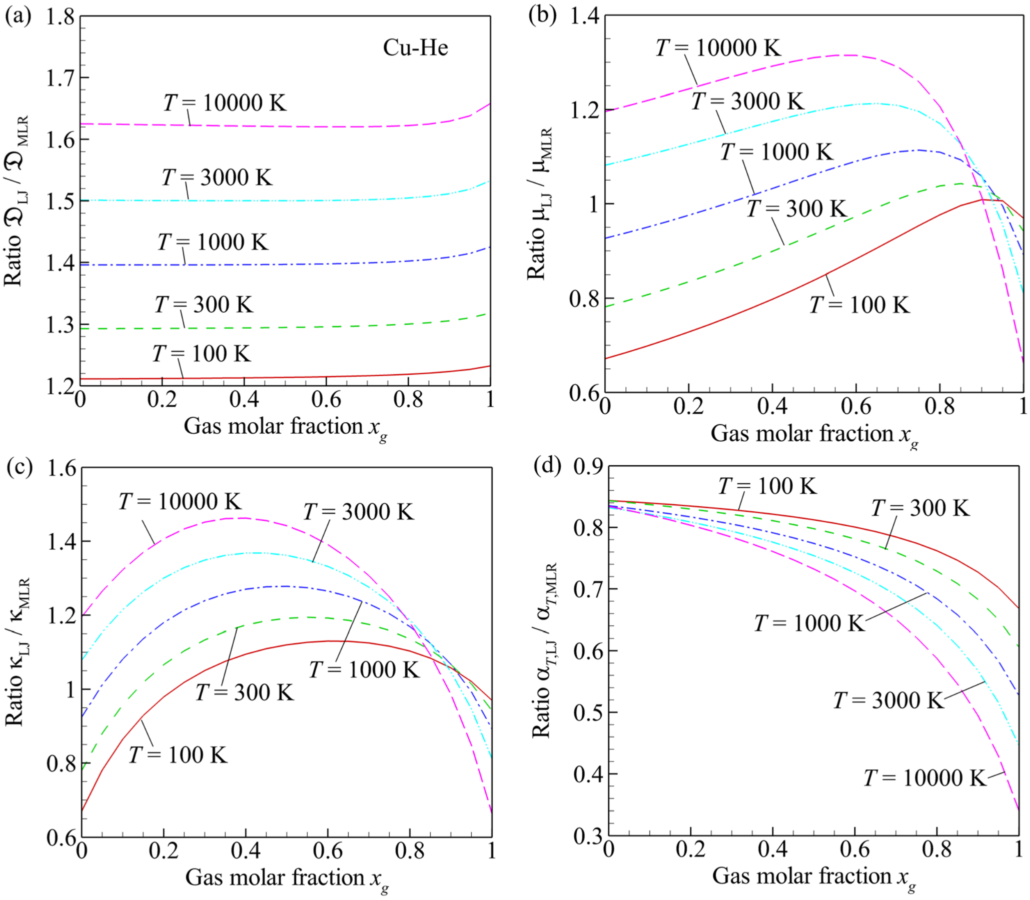

Fig. 13 Ratios of binary diffusivities $\mathfrak{D}_{LJ}/\mathfrak{D}_{MLR}$ (a), viscosities μ_{LJ}/μ_{MLR} (b), thermal conductivities κ_{LJ}/κ_{MLR} (c), and thermal diffusion factors $\alpha_{T,LJ}/\alpha_{T,MLR}$ (d) calculated based on the LJ (subscripts "LJ") and MLR (subscripts "MLR") potentials for the Cu–He mixture *versus* gas molar fraction x_g at a temperature of T = 100 K (red solid curves), 300 K (green dashed curves), 1000 K (blue dashed-dotted curves), 3000 K (cyan dashed-double-dotted curves), and 10 000 K (magenta long-dashed curves).

squares fit of eqn (38) to the viscosity data in some temperature range $T_{f,min} \leq T \leq T_{f,max}$ and then the value of $d_{VHS,ref}$ is determined to exactly fit the viscosity at a reference temperature, $\mu_{VHS,ref} = \mu_{ref}$ ($T_{f,min} \leq T_{ref} \leq T_{f,max}$), using eqn (41). Then the value of the viscosity index can be calculated based on the tabulated values of viscosity $\mu_i = \mu(T_i)$ (here $T_{f,min} \leq T_i \leq T_{f,max}$; $i = 1,\ldots,M$) as

$$\omega = \left[\sum_{i=1}^{M}\left(\log\frac{T_i}{T_{ref}}\right)^2\right]^{-1}\sum_{i=1}^{M}\left[\left(\log\frac{\mu_i}{\mu_{ref}}\right)\left(\log\frac{T_i}{T_{ref}}\right)\right]. \quad (43)$$

To validate this approach, it was applied for noble gases in a short temperature range at $T_{f,min}$ = 270 K, $T_{f,max}$ = 500 K, and T_{ref} = 273 K. The obtained parameters of the VHS model are found to be in close agreement with the parameters obtained in ref. 22 for the same T_{ref}. In particular, for argon gas, the present calculations result in values of $d_{VHS,ref}$ = 4.195 Å and ω = 0.81, which practically coincide with the values of $d_{VHS,ref}$ = 4.19 Å and ω = 0.81 in ref. 22.

The calculated values of viscosity for various atom pairs, however, do not exactly follow the power laws in the whole range of temperature under consideration. The range of temperature from 10 K to 10^4 K can contain up to three sub-ranges, where the best-fit ω significantly changes. For instance, for argon, the viscosity approximately follows power laws $\mu \propto T^{0.776}$ at 10 K $\leq T \leq$ 70 K, $\mu \propto T^{0.902}$ at 70 K $\leq T \leq$ 500 K, and $\mu \propto T^{0.683}$ at 500 K $\leq T \leq 10^4$ K. The same trend is also characteristic, *e.g.*, for viscosity contribution of Si–Ar collisions [Fig. 9(e)]. For other atom pairs, it can be sufficient to divide the range of temperature under consideration only in two sub-ranges, *e.g.*, for contributions of Cu–Cu collisions, or a good power fit can be obtained in the whole temperature range, *e.g.*, for contributions of Si–Si collisions [Fig. 8(a)].

Taking into account the diversity in the variation of viscosity with temperature for different atom pairs, we developed at least two parametrizations of the VHS model for each pair, which are different by the boundaries of $T_{f,min}$ and $T_{f,max}$ of the fitting temperature range and by T_{ref}. In the first parametrization, ω is obtained by fitting the viscosity data in the range from $T_{f,min}$ = 300 K to $T_{f,max} = 10^4$ K at T_{ref} = 300 K, or, in some cases, if the lower boundary can be reduced without sacrificing the accuracy, from $T_{f,min}$ = 100 K. In the second parametrization, ω is fitted in the range from $T_{f,min} = 10^3$ K to $T_{f,max} = 10^4$ K at $T_{ref} = 10^3$ K.

The reference values of the transport coefficients that are calculated based on the MLR potentials with the one-term

Table 5 Self (for single-species atom pairs) or binary (for mixed-species pairs A–B composed of different atoms A and B) diffusivity $\mathfrak{D}_{\mathrm{ref}}$ (at a number density of $n = 10^{19}$ cm^{-3}), viscosity μ_{ref}, thermal conductivity κ_{ref}, and HS diameter $d_{\mathrm{HS,ref}}$ [eqn (41) at $\omega = 1/2$] at the reference temperature T_{ref} calculated based on the one-term expansions with respect to the Sonine polynomials, and MLR potentials

Atomic pair	T_{ref} (K)	$\mathfrak{D}_{\mathrm{ref}}$ (mm^2 s^{-1})	μ_{ref} (μPa s)	κ_{ref} (mW m^{-1} K^{-1})	$d_{\mathrm{HS,ref}}$ (Å)
He–He	3×10^2	412.9	19.79	154.2	2.162
	10^3	980.8	45.71	356.1	1.922
Ar–Ar	3×10^2	45.22	22.65	17.68	3.592
	10^3	11.24	55.30	43.16	3.106
Xe–Xe	3×10^2	14.25	23.22	5.515	4.776
	10^3	39.66	64.78	15.38	3.864
Cu–Cu	3×10^2	18.65	14.74	72.32	5.001
	10^3	40.37	33.86	16.61	4.448
Cu–He	3×10^2	88.27	85.43	35.37	3.854
	10^3	179.9	17.31	71.69	3.658
Cu–Ar	3×10^2	43.44	25.98	16.51	3.531
	10^3	114.9	67.30	42.77	2.964
Cu–Xe	3×10^2	14.75	16.77	6.107	5.051
	10^3	53.10	55.52	20.21	3.751
Si–Si	3×10^2	16.00	6.216	6.901	6.279
	10^3	41.73	16.50	18.31	5.208
Si–He	3×10^2	193.4	16.44	73.16	2.728
	10^3	482.9	39.98	177.9	2.364
Si–Ar	3×10^2	39.13	15.79	14.93	4.101
	10^3	130.4	52.95	50.05	3.026
Si–Xe	3×10^2	18.27	11.26	7.588	5.285
	10^3	61.60	35.50	23.92	4.022

expansions with respect to the Sonine polynomials at T_{ref} = 300 K and $T_{\mathrm{ref}} = 10^3$ K are presented in Table 5. This table also includes the values of the HS molecular diameter $d_{\mathrm{HS,ref}}$ calculated at $T = T_{\mathrm{ref}}$ using eqn (41) with $\omega = 1/2$.

The calculated values of the VHS model parameters are given in Table 6 along with the quantities $\Delta[\ldots]_{\mathrm{A}}$ and $\Delta[\ldots]_{\mathrm{M}}$ which are equal to the RMS and maximum relative differences between the diffusivities ($\Delta[\mathfrak{D}]_{\mathrm{A}}$ and $\Delta[\mathfrak{D}]_{\mathrm{M}}$) and viscosities ($\Delta[\mu]_{\mathrm{A}}$ and $\Delta[\mu]_{\mathrm{M}}$) calculated based on eqn (37) and (38) and corresponding transport coefficients calculated based on the MLR potentials. For cross-species collisions, the differences in Table 6 characterize the differences between the contributions of corresponding collisions calculated based on the VHS model and MLR potentials using the one-term expansions with respect to the Sonine polynomials and do not represent the differences between the transport coefficients of corresponding gas mixtures.

The VHS model cannot fit, however, the diffusion coefficient with the same accuracy as the viscosity and thermal conductivity, since eqn (39) does not include any adjustable parameter that can be changed to enforce the agreement between $\mathfrak{D}_{\mathrm{VHS,ref}}$ and $\mathfrak{D}_{\mathrm{ref}}$, while $\mathfrak{D}$ and μ are defined by different Ω-integrals in eqn (22) and (23). This well-known deficiency of the VHS model results in relatively large RMS deviations $\Delta[\mathfrak{D}]_{\mathrm{A}}$ of diffusivity, which are on the order of 10–30% for all atom pairs (Table 6).

7.2. Variable soft sphere (VSS) model

The failure of the VHS model in predicting correct values of diffusivity is one of the major flaws of this model. To solve this problem, it was suggested[27] to modify the VHS model by introducing non-isotropic scattering of particles in binary collisions, when the deflection angle is defined by the equation

$$\chi(C_r, b) = 2\arccos\left[\left(\frac{b}{d_{\mathrm{VSS}}(C_r)}\right)^{1/\alpha}\right], \tag{44}$$

where the molecular diameter $d_{\mathrm{VSS}}(C_r)$ is defined likewise the VHS model as

$$d_{\mathrm{VSS}} = d_{\mathrm{VSS,ref}}\left(\frac{C_{r,\mathrm{ref}}}{C_r}\right)^{\omega-1/2}. \tag{45}$$

In this VSS model, α is an additional parameter that is chosen to fit the gas diffusivity.

By inserting eqn (44) into eqn (14), one can prove that, in the VSS model, the dependences of diffusivity, viscosity, and thermal conductivity are defined by the power laws in the form of eqn (37)–(39), but the reference values depend on α:

$$\mathfrak{D}_{\mathrm{VSS,ref}} = \frac{(\alpha+1)}{2}\frac{3\sqrt{\pi}}{8\Gamma(7/2-\omega)\pi d_{\mathrm{VHS,ref}}{}^2 n_{\mathrm{ref}} C_{r,\mathrm{ref}}^{2\omega-1}}\left(\frac{2k_{\mathrm{B}}T_{\mathrm{ref}}}{m}\right)^{\omega}, \tag{46}$$

$$\mu_{\mathrm{VSS,ref}} = \frac{(\alpha+1)(\alpha+2)}{6\alpha}\frac{15m}{(5-2\omega)(7-2\omega)d_{\mathrm{VSS,ref}}{}^2}\sqrt{\frac{k_{\mathrm{B}}T_{\mathrm{ref}}}{2\pi m}}, \tag{47}$$

$$\kappa_{\mathrm{VSS,ref}} = \frac{\bar{c}_{\mathrm{p}}\mu_{\mathrm{VSS,ref}}}{\overline{\mathrm{Pr}}}. \tag{48}$$

Then the calculation of the VSS model parameters can be implemented as follows. First, likewise the VHS model, the viscosity index can be calculated based on eqn (43), assuming that $\mu_{\mathrm{VSS,ref}} = \mu_{\mathrm{ref}}$. This results in the same ω for the VHS and VSS models if the same viscosity data are used in both cases. Then $d_{\mathrm{VSS,ref}}$ and α can be found from the conditions $\mu_{\mathrm{VSS,ref}} = \mu_{\mathrm{ref}}$ and $\mathfrak{D}_{\mathrm{VSS,ref}} = \mathfrak{D}_{\mathrm{ref}}$. These conditions reduce to

$$\alpha = \frac{10}{3(7/2-\omega)\mathrm{Sc}_{\mathrm{ref}} - 5}, \tag{49}$$

where $\mathrm{Sc}_{\mathrm{ref}} = \mu_{\mathrm{ref}}/(\mathfrak{D}_{\mathrm{ref}} n_{\mathrm{ref}} m)$. Once α is determined from eqn (49), the molecular diameter can be found from eqn (47).

The calculated values of the VSS model parameters are given in Table 6. The viscosities of Cu and Si vapor calculated based on the VSS [dashed-dotted curves in Fig. 8(a)] deviate from the viscosities predicted based on the MLR potentials within 1–7% and 1%, respectively. These relatively small differences are realized because the viscosity index ω is defined by eqn (43) to provide the least squares fit of viscosity in a broad range of temperature. As one can see, the VSS model compared to the VHS model allows one to reduce the RMS error in diffusivity from 10–30% to 0.5–5%.

The ratios of the transport coefficients calculated with the one-term Sonine polynomial expansions based on the VSS model and MLR potentials are compared in Fig. 14 for Cu–He mixture. In this case study, the differences between the results based on the VSS model and MLR potential do not exceed 8%. With exception of large temperatures, $T \gtrsim 7000$ K, the largest differences are observed at large molar fractions of helium.

Table 6 Parameters of the VHS and VSS molecular models [diameter $d_{\text{MM,ref}}$ at the reference temperature T_{ref}, viscosity index ω, and parameter α in eqn (34), (44) and (45); MM = VHS or VSS]. The values of ω are calculated based on the least-square fitting of the viscosity calculated based on the one-term expansions with respect to the Sonine polynomials in the temperature range $T_{\text{f,min}} \le T \le T_{\text{f,max}}$. The quantities $\Delta[\ldots]_A$ and $\Delta[\ldots]_M$ are the RMS and maximum relative differences between the diffusivity $\Delta[\mathfrak{D}]_A$ and $\Delta[\mathfrak{D}]_M$ and viscosity $\Delta[\mu]_A$ and $\Delta[\mu]_M$ values predicted by the molecular models and the values calculated with the one-term expansions with respect to the Sonine polynomials. For mixed-species atom pairs A–B composed of different atoms A and B, the differences are calculated for contributions of corresponding cross-species collisions based on eqn (22) and (23). The star "*" marks the parametrizations of the VSS model, which are used to obtain the results presented in Fig. 8 and 14 and in the ESI

Atomic pair	Model	T_{ref} (K)	$d_{\text{MM,ref}}$ (Å)	ω	α	$T_{\text{f,min}}$ (K)	$T_{\text{f,max}}$ (K)	$\Delta[\mathfrak{D}]_A$ (%)	$\Delta[\mathfrak{D}]_M$ (%)	$\Delta[\mu]_A$ %	$\Delta[\mu]_M$ %
He–He	VHS	3×10^2	2.403	0.7400	—	3×10^2	10^4	25.1	31.5	4.08	6.61
		10^3	2.171	0.7740	—	10^3	10^4	26.4	30.6	2.37	4.27
	VSS*	3×10^2	2.368	0.7400	1.4402	3×10^2	10^4	7.62	13.9	4.08	6.61
		10^3	2.141	0.7740	1.5457	10^3	10^4	4.84	9.27	2.37	4.27
Ar–Ar	VHS	3×10^2	3.929	0.7055	—	3×10^2	10^4	20.1	20.8	1.68	4.67
		10^3	3.358	0.6796	—	10^3	10^4	19.2	21.3	0.43	0.87
	VSS*	3×10^2	3.876	0.7055	1.3055	3×10^2	10^4	5.30	6.09	1.68	4.67
		10^3	3.311	0.6796	1.3235	10^3	10^4	3.72	6.00	0.43	0.87
Xe–Xe	VHS	3×10^2	5.360	0.7607	—	3×10^2	10^4	21.8	26.5	4.74	10.5
		10^3	4.204	0.6938	—	10^3	10^4	19.2	20.5	0.44	1.07
	VSS	3×10^2	5.283	0.7607	1.3717	3×10^2	10^4	5.27	10.2	4.74	10.5
		10^3	4.140	0.6949	1.3136	10^3	10^4	3.98	5.46	0.44	1.07
Cu–Cu	VHS	3×10^2	5.427	0.6881	—	10^2	7×10^3	9.52	16.6	0.67	1.27
		3×10^2	5.446	0.6958	—	10^2	10^4	12.4	23.6	2.67	7.42
		10^3	4.833	0.6857	—	10^2	7×10^3	9.36	15.8	0.64	1.45
	VSS*	3×10^2	5.352	0.6881	1.3100	10^2	7×10^3	8.86	12.2	0.67	1.27
		3×10^2	5.371	0.6958	1.3159	10^2	10^4	9.31	14.3	2.67	7.42
		10^3	4.781	0.6857	1.1873	10^2	7×10^3	3.91	5.94	0.64	1.45
Cu–He	VHS	3×10^2	4.003	0.5891	—	10^2	10^4	10.8	11.4	0.20	0.37
		10^3	3.802	0.5908	—	10^2	10^4	10.9	11.3	0.15	0.68
	VSS*	3×10^2	3.962	0.5891	1.1742	10^2	10^4	1.06	1.62	0.20	0.37
		10^3	3.761	0.5908	1.1855	10^2	10^4	0.57	0.99	0.15	0.68
Cu–Ar	VHS	3×10^2	3.955	0.7566	—	3×10^2	10^4	22.0	24.3	1.83	4.28
		10^3	3.282	0.7317	—	10^3	10^4	21.0	21.3	0.14	0.30
	VSS*	3×10^2	3.898	0.7566	1.4116	3×10^2	10^4	3.55	5.99	1.83	4.28
		10^3	3.235	0.7317	1.4406	10^3	10^4	0.84	1.20	0.14	0.30
Cu–Xe	VHS	3×10^2	6.322	0.9832	—	3×10^2	10^4	27.0	33.1	7.00	12.0
		10^3	4.672	0.9706	—	10^3	10^4	27.4	32.6	6.68	10.3
	VSS	3×10^2	6.241	0.9832	1.4131	3×10^2	10^4	10.6	16.9	7.00	12.0
		10^3	4.615	0.9706	1.6238	10^3	10^4	5.95	9.40	6.68	10.3
Si–Si	VHS	3×10^2	7.211	0.8093	—	10^2	10^4	11.3	17.4	0.35	1.28
		10^3	5.979	0.8085		10^2	10^4	11.2	17.4	0.37	1.30
	VSS*	3×10^2	7.134	0.8093	1.1831	10^2	10^4	3.16	7.90	0.35	1.28
		10^3	5.923	0.8085	1.1511	10^2	10^4	3.84	9.46	0.37	1.30
Si–He	VHS	3×10^2	3.071	0.7292	—	3×10^2	10^4	19.0	22.3	1.79	3.17
		10^3	2.605	0.7217	—	10^3	10^4	18.7	21.6	1.53	2.50
	VSS	3×10^2	2.974	0.7292	1.3991	3×10^2	10^4	3.12	5.67	1.79	3.17
		10^3	2.568	0.7230	1.4572	10^3	10^4	4.08	7.80	1.53	2.50
Si–Ar	VHS	3×10^2	4.834	0.8628	—	3×10^2	10^4	25.2	34.2	8.22	15.8
		10^3	3.391	0.7577	—	10^3	10^4	20.7	22.5	2.08	3.64
	VSS	3×10^2	4.767	0.8628	1.5018	3×10^2	10^4	7.90	15.3	8.22	15.8
		10^3	3.342	0.7577	1.3894	10^3	10^4	2.89	4.65	2.08	3.64
Si–Xe	VHS	3×10^2	6.555	0.9627	—	3×10^2	10^4	25.6	29.3	4.26	8.31
		10^3	4.997	0.9661	—	10^3	10^4	26.4	29.9	4.62	8.01
	VSS	3×10^2	6.461	0.9627	1.3869	3×10^2	10^4	9.13	13.1	4.26	8.31
		10^3	4.931	0.9661	1.5618	10^3	10^4	4.83	7.76	4.62	8.01

It occurs because the VSS model parameterization used to obtain results in Fig. 14 provides relatively large errors with respect to the MLR potential even in the case of pure helium gas. At $T \gtrsim 7000$ K, the VSS model parametrization for Cu vapor also becomes relatively inaccurate. Interestingly, the comparison of results in Fig. 13 and 14 shows that the use of the LJ potentials, on average, results in order-of-magnitude higher errors in the transport properties of the Cu–He mixture compared to the VSS molecular model.

The calculations of the transport coefficients based on the VSS model for other gas mixtures reveal the same trends and a similar average level of discrepancy on the order of $\sim$10% with respect to the values predicted based on the MLR potential. The magnitude of error, however, ultimately depends on the accuracy of the approximation of the Ω-integrals by power functions of temperature over the whole temperature range considered. The accuracies of such approximations in a broad temperature range strongly vary for different atom pairs (Fig. 7). As a result, the transport coefficients of some mixtures, when calculated based on the VSS model, can exhibit relatively large magnitudes of error in certain temperature ranges. For instance, the calculations for the Cu–Ar mixture indicate the maximum errors in $\mathfrak{D}$, μ, and κ of $\sim$8% at $T \geq 300$ K, while the errors can rise to $\sim$30% at $T = 100$ K.[85] At this temperature, the thermal

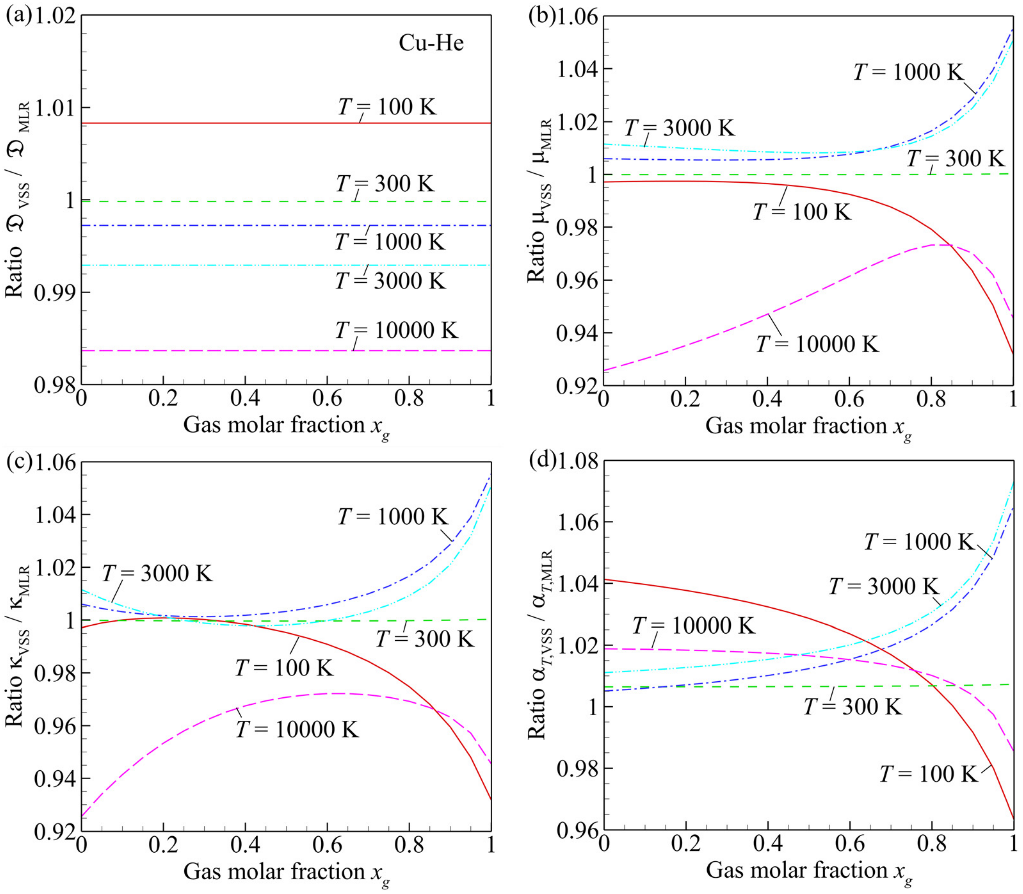

Fig. 14 Ratios of binary diffusivities $\mathfrak{D}_{VSS}/\mathfrak{D}_{MLR}$ (a), viscosities μ_{VSS}/μ_{MLR} (b), thermal conductivities $\kappa_{VSS}/\kappa_{MLR}$ (c), and thermal diffusion factors $\alpha_{T,VSS}/\alpha_{T,MLR}$ (d) calculated based on the VSS molecular model with the parameterizations marked with "*" in Table 6 (subscripts "VSS") and MLR potential (subscripts "MLR") for the Cu–He mixture *versus* gas molar fraction x_g at a temperature of T = 100 K (red solid curves), 300 K (green dashed curves), 1000 K (blue dashed-dotted curves), 3000 K (cyan dashed-double-dotted curves), and 10 000 K (magenta long-dashed curves). All transport coefficients are calculated based on the one-term expansions with respect to the Sonine polynomials.

diffusion factor predicted based on the VSS model is three-fold different from α_T calculated based on the MLR potentials and has the opposite sign. This suggests that the prediction of the thermal diffusion effects based on the VSS model can be qualitatively wrong and any calculations of thermal diffusion based on the VHS and VSS molecular models must be accompanied by a careful analysis of the errors associated with a particular choice of the model parameters.

For pure substances, eqn (37)–(39) with parameters in Tables 5 and 6 provide the first-order power-law approximations of all transport coefficients. For gas mixtures, eqn (37) can be used directly for binary diffusivity, while the power-law approximations in eqn (38) and (39) for single- and cross-species contributions should be used together with eqn (25)–(27). The final algebraic form of eqn (25)–(27) is given, *e.g.*, in ref. 24.

8. Conclusions

The quantum Monte Carlo (QMC) calculations of the potential energy curves (PECs) are performed in a broad range of interatomic (internuclear) distances for the He–He, Ar–Ar, Cu–Cu, Cu–He, Cu–Ar, Cu–Xe, Si–Si, Si–He, Si–Ar, and Si–Xe dimers. The QMC method is found to be a robust and reliable tool for *ab initio* prediction of interaction in dimers with van der Waals, covalent, and metallic bonding. The results obtained in the QMC calculations are found to be in close quantitative agreement with the results of the state-of-the-art CCSD(T) calculations and spectroscopic measurements. The *ab initio* PECs are used to obtain fitting parameters for the Morse long range (MLR) potential function for all dimers considered. The calculated potential well depth and equilibrium interatomic distance can be also used to approximate the *ab initio* PECs by semi-empirical (12-6) Lennard-Jones (LJ) potentials. It is found that the LJ potential, as a rule, strongly overestimates the magnitude of the interatomic force at repulsion. The case of the Cu–He dimer, where the LJ potential underestimates the force at the repulsive PEC branch, is an exception to this rule. The LJ potential also strongly overestimates the attractive forces in the homonuclear Cu–Cu and Si–Si dimers.

The obtained MLR potentials are used to study the scattering of particles in binary collisions. This study showed that the shape and parameters of the PECs strongly affect the deflection angle in binary collisions at small collision speeds, when the outcomes of collisions depend on details of the asymptotic behavior of PECs at large interatomic distances. At moderate and large collision speeds, the values of the deflection angle predicted by different *ab initio* PECs for noble gases agree well with each other. The values of the deflection angle predicted based on the LJ potentials agree with MLR-based calculations only at moderate speeds and strongly disagree at both small and high speeds.

The obtained MLR and LJ potentials are used to calculate diffusivity, viscosity, thermal conductivity, and thermal diffusion factor (for mixtures) of helium, argon, and xenon gases, copper and silicon vapors, as well as corresponding mixtures of vapors with the noble gases in the form of one-, two-, and ten-term expansions with respect to the Sonine polynomials in the framework of the Chapman–Enskog method. For pure substances, the PEC shape is found to strongly affect the contributions of corresponding binary collisions, measured either in terms of the transport collision integrals or transport coefficients in the form of one-term expansions with respect to the Sonine polynomials, at small and large (compared to the room temperature) temperatures. For the Cu–Cu and Cu–He atom pairs, the values of the transport collisions integrals and transport coefficients calculated based on the LJ and MLR potentials are strongly different practically in the whole temperature range from 100 K to 10 000 K. For high-temperature binary mixtures, the errors in the values of the transport coefficients calculated based on the LJ potentials can be as high as 30–60%. This suggests that the LJ approximation is not suitable for predicting the transport properties of high-temperature gases and gaseous mixtures considered in the present work.

The present study also reveals some intriguing and abnormal behavior of the transport coefficients in the mixtures of copper or silicon vapors with noble gases. In particular, it was found that the mixture viscosity and thermal conductivity can be larger than the viscosity and thermal conductivity of corresponding pure substances at the same temperature. The simulations also reveal a large magnitude of the thermal diffusion factor in Cu–He and Si–He mixtures, which can be up to 300% larger than the magnitude of the thermal diffusion factor in binary mixtures containing heavier noble gases. This finding implies that the thermal diffusion, which is often assumed to be negligible, can affect, *e.g.*, the structure of mixing layers between high-temperature vapor plumes and cold helium background gas.

Finally, the transport coefficients calculated with the one-term expansions with respect to the Sonine polynomials were used to find parameters of the variable hard sphere (VHS) and variable soft sphere (VSS) molecular models, which are routinely used in the direct simulation Monte Carlo (DSMC) simulations of rarefied gas flows. The errors in the transport coefficients, when the VSS model parametrizations developed in the present work are used, are smaller than 10% at room and higher temperatures for pure substances and gaseous mixtures.

The comprehensive results obtained in the present work on the collisional properties, transport coefficients, and VHS/VSS molecular model parameters contain *all* necessary information that is required for sampling binary collisions in kinetic, including DSMC, simulations and calculations of the transport coefficients in continuum simulations of high-temperature flows of copper and silicon vapors, as well as their mixtures with helium, argon, and xenon gases.

Author contributions

Kevin W. Kayang: Data curation (equal); formal analysis (lead); investigation (lead); software (equal); visualization (equal); writing/original draft preparation (equal); writing/review & editing (equal). Alexey N. Volkov: conceptualization (lead); data curation (equal); methodology (equal); software (equal); supervision (lead); visualization (equal); writing/original draft preparation (equal); writing/review & editing (lead). Petr A. Zhilyaev: methodology (equal); validation (lead); writing/original draft preparation (equal); writing/review & editing (equal). Felix Sharipov: data curation (equal); methodology (equal); software (equal); validation (equal); writing/original draft preparation (equal); writing/review & editing (equal).

Conflicts of interest

The authors have no conflicts to disclose.

Appendices

Appendix. Tabulated PECs and transport coefficients of Cu and Si vapors

The selected values of energy found in the QMC calculations performed in the present work are presented in Table 7 for the

Table 7 Energy (eV) of the homonuclear and heteronuclear dimers involving Cu and Si atoms found in the QMC calculations

Distance	Dimer			
r (Å)	Cu–Cu	Cu–He	Cu–Ar	Cu–Xe
0.6	5.145×10^{2}	—	—	—
1.4	1.128×10^{1}	—	4.225×10^{2}	2.927×10^{1}
1.8	-5.171×10^{-1}	—	9.613	5.513
2.4	-2.038	1.999×10^{2}	4.437×10^{-1}	2.094×10^{-1}
3	-1.145	4.396	4.597×10^{-2}	-1.175×10^{-1}
3.6	-4.078×10^{-1}	9.234×10^{-2}	-5.470×10^{-3}	-8.301×10^{-2}
4.2	-1.092×10^{-1}	7.341×10^{-4}	-9.802×10^{-3}	-4.273×10^{-2}
4.8	-2.768×10^{-2}	-7.418×10^{-4}	-6.357×10^{-3}	-2.006×10^{-2}
5.4	-7.079×10^{-3}	-4.429×10^{-4}	-3.379×10^{-3}	-9.324×10^{-3}
6	-1.733×10^{-3}	-2.860×10^{-4}	-1.626×10^{-3}	-4.518×10^{-3}
7	-7.091×10^{-4}	-1.302×10^{-4}	-3.853×10^{-4}	-1.557×10^{-3}
	Si–Si	Si–He	Si–Ar	Si–Xe
0.6	1.762×10^{2}	—	—	—
1.3	1.464×10^{1}	3.012×10^{2}	7.222×10^{2}	4.874×10^{1}
1.8	-1.320	1.166	9.510	7.865
2.4	-3.163	5.655×10^{-2}	3.624×10^{-1}	4.490×10^{-1}
3	-1.611	-3.216×10^{-3}	-1.783×10^{-2}	-1.811×10^{-1}
3.6	-5.795×10^{-1}	-4.831×10^{-3}	-3.328×10^{-2}	-9.721×10^{-2}
4.2	-2.145×10^{-1}	-2.740×10^{-3}	-1.751×10^{-2}	-4.346×10^{-2}
4.8	-8.892×10^{-2}	-1.292×10^{-3}	-8.207×10^{-3}	-2.342×10^{-2}
5.4	-4.117×10^{-2}	-5.571×10^{-4}	-3.921×10^{-3}	-1.383×10^{-2}
6	-2.082×10^{-2}	-2.368×10^{-4}	-1.884×10^{-3}	-7.922×10^{-3}
7	-7.854×10^{-3}	-6.264×10^{-5}	-4.669×10^{-4}	-2.056×10^{-3}

Table 8 Self-diffusivity $\mathfrak{D}$, viscosity μ, and thermal conductivity κ of Si and Cu vapors as functions of temperature T. The self-diffusivity is calculated at a pressure of 1 atm = 101 325 Pa

	Cu vapor			Si vapor		
T (K)	$\mathfrak{D}$ (mm^2 s^{-1})	μ (μPa s)	κ (mW m^{-1} K^{-1})	$\mathfrak{D}$ (mm^2 s^{-1})	μ (μPa s)	κ (mW m^{-1} K^{-1})
100	1.21057	6.9141	3.4034	0.89967	2.5393	2.8223
200	3.89895	11.199	5.5133	3.15576	4.4754	4.9744
300	7.67887	14.824	7.2983	6.55939	6.2272	6.9218
400	12.3787	18.080	8.9015	11.0111	7.8679	8.7456
1000	55.5734	34.066	16.771	57.0452	16.525	18.370
1400	95.9998	43.048	21.192	104.305	21.684	24.104
2000	171.536	55.201	27.174	198.0340	28.912	32.140
2400	231.176	62.618	30.830	275.167	33.492	37.232
3000	334.275	72.821	35.869	412.311	40.101	44.578
3400	412.354	79.084	38.966	517.892	44.366	49.319
4000	544.435	87.886	43.314	697.443	50.585	56.232
4400	643.185	93.506	46.083	831.341	54.625	60.724
5000	808.707	101.80	50.154	1053.80	60.545	67.306
5400	931.445	107.34	52.868	1216.78	64.409	71.603
6000	1135.45	115.82	57.011	1483.92	70.106	77.936
6400	1285.44	121.65	59.852	1677.54	73.853	82.100
7000	1532.56	130.70	64.267	1992.11	79.424	88.288
7400	1712.69	136.97	67.327	2218.43	83.120	92.392
8000	2006.94	146.75	72.103	2583.77	88.666	98.546
8400	2219.68	153.53	75.416	2845.11	92.377	102.66
9000	2564.49	164.07	80.579	3264.76	97.985	108.88
9400	2811.94	171.36	84.148	3563.52	101.76	113.07
10 000	3210.21	182.65	89.690	4041.07	107.50	119.43

homonuclear and heteronuclear dimers involving Cu and Si atoms. For Cu and Si vapors, the selected values of self-diffusivity, viscosity, and thermal conductivity calculated based on the MLR potentials with the ten-term expansions with respect to the Sonine polynomials are presented in Table 8. The corresponding tables, containing all values obtained in calculations, are provided in the ESI.†

Acknowledgements

K. W. K. and A. N. V. acknowledge the support from MKS Instruments, Inc. and NSF through award CMMI-1554589 and RII-Track-1 Future Technologies and Enabling Plasma Processes project (award OIA-2148653). F. S. thanks CNPq, Brazil, for the support of his research (Grant No. 304831/2018-2). The computational support is provided by the Alabama Supercomputer Center.

References

1 N. B. Dahotre and S. P. Harimkar, *Laser Fabrication and Machining of Materials*, Springer, New York, 2008.

2 S. Ly, A. M. Rubenchik, S. A. Khairallah, G. Giss and M. J. Matthews, Metal vapor micro-jet controls material redistribution in laser powder bed fusion additive manufacturing, *Sci. Rep.*, 2017, **7**, 4085.

3 P. R. Willmott and J. R. Huber, Pulsed laser vaporization and deposition, *Rev. Mod. Phys.*, 2000, **72**, 315–328.

4 M. Mahjouri-Samani, M. Tian, A. A. Puretzky, M. Chi, K. Wang, G. Duscher, C. M. Rouleau, G. Eres, M. Yoon, J. Lasseter, K. Xiao and D. B. Geohegan, Nonequilibrium synthesis of TiO_2 nanoparticle "building blocks" for crystal growth by sequential attachment in pulsed laser deposition, *Nano Lett.*, 2017, **17**, 4624–4633.

5 A. Ojeda-G-P, M. Döbeli and T. Lippert, Influence of plume properties on thin film composition in pulsed laser deposition, *Adv. Mater. Interfaces*, 2018, **5**, 1701062.

6 D. B. Geohegan, A. A. Puretzky, G. Duscher and S. J. Pennycook, Time-resolved imaging of gas phase nanoparticle synthesis by laser ablation, *Appl. Phys. Lett.*, 1998, **72**, 2987–2989.

7 D. W. Hahn and N. Omenetto, Laser-induced breakdown spectroscopy (LIBS), part I: Review of basic diagnostics and plasma–particle interactions: Still-challenging issues within the analytical plasma community, *Appl. Spectrosc.*, 2010, **64**, 335A–366A.

8 O. Ellegaard and J. Schou, Ablation of volatile films by laser heating of substrates, *J. Appl. Phys.*, 1998, **83**, 1078–1086.

9 J. R. Ho, C. P. Grigoropoulos and J. A. C. Humphrey, Gas dynamics and radiation heat transfer in the vapor plume produced by pulsed laser irradiation of aluminum, *J. Appl. Phys.*, 1996, **79**, 7205–7215.

10 T. E. Itina, W. Marine and M. Autric, Mathematical modelling of pulsed laser ablated flows, *Appl. Surf. Sci.*, 2000, **154–155**, 60–65.

11 V. I. Mazhukin, V. V. Nossov and I. Smurov, Modeling of plasma-controlled evaporation and surface condensation of Al induced by 1.06 and 0.248 μm laser radiations, *J. Appl. Phys.*, 2007, **101**, 024922.

12 S. S. Harilal, G. V. Miloshevsky, P. K. Diwakar, N. L. LaHaye and A. Hassanein, Experimental and computational study of complex shockwave dynamics in laser ablation plumes in argon atmosphere, *Phys. Plasmas*, 2012, **19**, 083504.

13 S. B. Harris, J. H. Paiste, T. J. Holdsworth, R. R. Arslanbekov and R. P. Camata, Laser-generated plasmas in length scales relevant for thin film growth and processing: Simulation and experiment, *J. Phys. D: Appl. Phys.*, 2019, **53**(1), 015203.

14 D. Sibold and H. M. Urbassek, Kinetic study of pulsed desorption flows into vacuum, *Phys. Rev. A: At., Mol., Opt. Phys.*, 1991, **43**, 6722–6734.

15 T. E. Itina, A. A. Katassonov, W. Marine and M. Autric, Numerical study of the role of a background gas and system geometry in pulsed laser deposition, *J. Appl. Phys.*, 1998, **83**, 6050–6054.

16 A. N. Volkov, G. M. O'Connor, T. J. Glynn and G. A. Lukyanov, Expansion of a laser plume from a silicon wafer in a wide range of ambient gas pressures, *Appl. Phys. A: Mater. Sci. Process.*, 2008, **92**, 927–932.

17 A. Palya, O. A. Ranjbar, Z. Lin and A. N. Volkov, Kinetic simulations of laser-induced plume expansion into a background gas under conditions of spatial confinement, *Int. J. Heat Mass Transfer*, 2019, **132**, 1029–1052.

18 O. A. Ranjbar, Z. Lin and A. N. Volkov, Plume accumulation effect and interaction of plumes induced by irradiation of a copper target with a burst of nanosecond laser pulses near the ionization threshold, *J. Appl. Phys*, 2020, **127**, 223105.

19 M. A. Stokes, S. A. Khairallah, A. N. Volkov and A. M. Rubenchik, Fundamental physics effects of background gas species and pressure on vapor plume structure and spatter entrainment in laser melting, *Additive Manuf.*, 2022, **55**, 102819.

20 V. A. Petrov, O. A. Ranjbar, P. A. Zhilyaev and A. N. Volkov, Kinetic simulations of laser-induced plume expansion from a copper target into a vacuum or argon background gas based on ab initio calculation of Cu–Cu, Ar–Ar, and Ar–Cu interactions, *Phys. Fluids*, 2020, **32**(10), 102010.

21 A. N. Volkov, Splitting of laser-induced neutral and plasma plumes: Hydrodynamic origin of bimodal distributions of vapor density and plasma emission intensity, *J. Phys. D: Appl. Phys.*, 2021, **54**, 37LT01.

22 G. A. Bird, *Molecular Gas Dynamics and the Direct Simulation of Gas Flows*, Oxford University Press, New York, 1994.

23 S. Chapman and T. G. Cowling, *The Mathematical Theory of Non-Uniform Gases*, University Press, Cambridge, 1952.

24 O. Hirschfelder, C. F. Curtiss and R. B. Bird, *The Molecular Theory of Gases and Liquids*, Wiley, New York, 1954.

25 J. H. Ferziger and H. G. Kaper, *Mathematical Theory of Transport Processes in Gases*, North-Holland Publishing Company, 1972.

26 G. A. Bird, Monte Carlo simulation in an engineering context, *Progr. Astro. Aero.*, 1981, **74**(1), 239–255.

27 K. Koura and H. Matsumoto, Variable soft sphere molecular model for inverse-power-law or Lennard-Jones potential, *Phys. Fluids A*, 1991, **3**, 2459–2465.

28 J. Fan, I. D. Boyd and C. Shelton, Monte Carlo modeling of electron beam physical vapor deposition of yttrium, *J. Vac. Sci. Technol., A*, 2000, **18**, 2937–2945.

29 A. Venkattraman and A. A.Alexeenko, Direct simulation Monte Carlo modeling of e-beam metal deposition, *J. Vac. Sci. Technol., A*, 2010, **28**, 916–924.

30 F. Sharipov and V. J. Benites, Transport coefficients of argon and its mixtures with helium and neon at low density based on ab initio potentials, *Fluid Phase Equilib.*, 2019, **498**, 23–32.

31 F. Sharipov, *Rarefied Gas Dynamics. Fundamentals for Research and Practice*, Wiley-VCH, 2016.

32 F. Sharipov, Direct simulation Monte Carlo method based on ab initio potential: Recovery of transport coefficients of multi-component mixtures of noble gases, *Phys. Fluids*, 2022, **34**, 097114.

33 F. Sharipov and J. L. Strapasson, Direct simulation Monte Carlo method for an arbitrary intermolecular potential, *Phys. Fluids*, 2012, **24**, 011703.

34 A. Venkattraman and A. A. Alexeenko, Binary scattering model for Lennard-Jones potential: Transport coefficients and collision integrals for non-equilibrium gas flow simulations, *Phys. Fluids*, 2012, **24**, 027101.

35 F. Claeyssens, S. J. Henley and M. N. R. Ashfold, Comparison of the ablation plumes arising from ArF laser ablation of graphite, silicon, copper, and aluminum in vacuum, *J. Appl. Phys.*, 2003, **94**, 2203–2211.

36 Z. Zeng, X. L. Mao, R. Greif and R. E. Russo, Experimental investigation of ablation efficiency and plasma expansion during femtosecond and nanosecond laser ablation of silicon, *Appl. Phys. A: Mater. Sci. Process.*, 2005, **80**, 237–241.

37 N. Farid, S. S. Harilal, H. Ding and A. Hassanein, Emission features and expansion dynamics of nanosecond laser ablation plumes at different ambient pressures, *J. Appl. Phys.*, 2014, **115**, 033107.

38 H. Yuan, A. B. Gojani, I. B. Gornushkin, X. Wang, D. Liu and M. Rong, Dynamics of laser-induced plasma splitting, *Opt. Lasers Eng.*, 2020, **124**, 105832.

39 S. Traore, M. Schneider, I. Koutiri, F. Coste, R. Fabbro, C. Charpentier, P. Lefebvre and P. Peyre, Influence of gas atmosphere (Ar or He) on the laser powder bed fusion of a Ni-based alloy, *J. Mater. Process. Technol.*, 2021, **288**, 116851.

40 A. K. Dham, W. J. Meath, A. R. Allnatt, R. A. Aziz and M. J. Slaman, XC and HFD-B Potential energy curves for Xe–Xe and related physical properties, *Chem. Phys.*, 1990, **142**, 173–189.

41 R. A. Aziz, A highly accurate interatomic potential for argon, *J. Chem. Phys.*, 1993, **99**(6), 4518–4525.

42 J. B. Anderson, An exact quantum Monte Carlo calculation of the helium–helium intermolecular potential. II, *J. Chem. Phys.*, 2001, **115**(10), 4546–4548.

43 K. Patkowski, G. Murdachaew, C. M. Fou and K. Szalewicz, Accurate ab initio potential for argon dimer including highly repulsive region, *Mol. Phys.*, 2005, **103**(15–16), 2031–2045.

44 R. Hellmann, E. Bich and E. Vogel, Ab initio potential energy curve for the helium atom pair and thermophysical properties of dilute helium gas. I. Helium–helium interatomic potential, *Mol. Phys.*, 2007, **105**(23–24), 3013–3023.

45 B. Jäger, R. Hellmann, E. Bich and E. Vogel, Ab initio pair potential energy curve for the argon atom pair and thermophysical properties of the dilute argon gas. I. Argon–argon interatomic potential and rovibrational spectra, *Mol. Phys.*, 2009, **107**(20), 2181–2188 [correction in Vol.108, 105 (2010)].

46 K. Patkowski and K. Szalewicz, Argon pair potential at basis set and excitation limits, *J. Chem. Phys.*, 2010, **133**, 094304.

47 W. Cencek, M. Przybytek, J. Komasa, J. B. Mehl, B. Jeziorski and K. Szalewicz, Effects of adiabatic, relativistic, and quantum electrodynamics interactions on the pair potential and thermophysical properties of helium, *J. Chem. Phys.*, 2012, **136**(22), 224303.

48 R. Hellmann, B. Jäger and E. Bich, State-of-the-art ab initio potential energy curve for the xenon atom pair and related spectroscopic and thermophysical properties, *J. Chem. Phys.*, 2017, **147**, 034304.

49 K. T. Tang and J. P. Toennies, An improved simple model for the van der Waals potential based on universal damping functions for the dispersion coefficients, *J. Chem. Phys.*, 1984, **80**(8), 3726–3741.

50 K. T. Tang and J. P. Toennies, The van der Waals potentials between all the rare gas atoms from He to Rn, *J. Chem. Phys.*, 2003, **118**(11), 4976–4983.

51 X. Sheng, J. P. Toennies and K. T. Tang, Conformal analytical potential for all the rare gas dimers over the full range of internuclear distances, *Phys. Rev. Lett.*, 2020, **125**, 253402.

52 E. Vogel, B. Jäger, R. Hellmann and E. Bich, Ab initio pair potential energy curve for the argon atom pair and thermophysical properties for the dilute argon gas. II. Thermophysical properties for low-density argon, *Mol. Phys.*, 2010, **108**(24), 3335–3352.

53 F. Sharipov and V. J. Benites, Transport coefficients of helium-argon mixture based on ab initio potential, *J. Chem. Phys.*, 2015, **143**, 154104.

54 F. Sharipov and V. J. Benites, Transport coefficients of helium-neon mixtures at low density computed from ab initio potentials, *J. Chem. Phys.*, 2017, **147**, 224302.

55 F. Sharipov and V. J. Benites, Transport coefficients of multi-component mixtures of noble gases based on ab initio potentials: Viscosity and thermal conductivity, *Phys. Fluids*, 2020, **32**, 077104.

56 F. Sharipov and V. J. Benites, Transport coefficients of multicomponent mixtures of noble gases based on ab initio potentials: Diffusion coefficients and thermal diffusion factors, *Phys. Fluids*, 2020, **32**, 097110.

57 F. Sharipov and V. J. Benites, Transport coefficients of isotopic mixtures of noble gases based on ab initio potentials, *Phys. Chem. Chem. Phys.*, 2021, **23**, 16664–161674.

58 R. F. Berg and W. C. Burton, Noble gas viscosities at 25 °C, *Mol. Phys.*, 2013, **111**(2), 195–199.

59 Y. Takahara, K. Yamaguchi and T. Fueno, Potential energy curves for transition metal dimers and complexes calculated by the approximately projected unrestricted Hartree-Fock and Møller-Plesset perturbation (APUMP) methods, *Chem. Phys. Lett.*, 1989, **158**(1–2), 95–101.

60 K. A. Peterson and C. Puzzarini, Systematically convergent basis sets for transition metals. II. Pseudopotential-based correlation consistent basis sets for the group 11 (Cu, Ag, Au) and 12 (Zn, Cd, Hg) elements, *Theor. Chem. Acc.*, 2005, **114**(4–5), 283–296.

61 A. W. Hauser, A. Volk, P. Thaler and W. E. Ernst, Atomic collisions in suprafluid helium-nanodroplets: timescales for metal-cluster formation derived from He-density functional theory, *Phys. Chem. Chem. Phys.*, 2015, **17**, 10805.

62 F. Cargnoni, T. Kuś, M. Mella and R. J. Bartlett, Ground state potential energy surfaces and bound states of M-He dimers: A theoretical investigation, *J. Chem. Phys.*, 2008, **129**, 204307.

63 X. F. Tong, C. L. Yang, Y. P. An, M. S. Wang, X. G. Ma and D. H. Wang, Theoretical characteristics of the bound states of MX complexes (M = Cu, Ag, and Au, and X = He, Ne, and Ar), *J. Chem. Phys.*, 2009, **131**(24), 244304.

64 D. A. Dixon, D. Feller, K. A. Peterson and J. L. Gole, The molecular structure and ionization potential of Si_2: The role of the excited states in the photoionization of Si_2, *J. Phys. Chem. A*, 2000, **104**(11), 2326–2332.

65 C. Tao, A. Teslja, P. J. Dagdigian, S. Atahan and M. H. Alexander, Laser spectroscopic study of the SiAr van der Waals complex, *J. Chem. Phys.*, 2002, **116**(21), 9239–9248.

66 R. J. Bartlett, Coupled-cluster approach to molecular structure and spectra: A step toward predictive quantum chemistry, *J. Phys. Chem.*, 1989, **93**(5), 1697–1708.

67 W. Kohn and L. J. Sham, Self-consistent equations including exchange and correlation effects, *Phys. Rev.*, 1965, **140**(4A), A1133.

68 T. Van Mourik and R. J. Gdanitz, A critical note on density functional theory studies on rare-gas dimers, *J. Chem. Phys.*, 2002, **116**(22), 9620–9623.

69 I. S. Gerasimov, T. V. Losev, E. Y. Epifanov, I. Rudenko, I. S. Bushmarinov, A. A. Ryabov, P. A. Zhilyaev and M. G. Medvedev, Comment on "Pushing the frontiers of density functionals by solving the fractional electron problem", *Science*, 2022, **377**(6606), eabp3385.

70 A. J. Cohen, P. Mori-Sánchez and W. Yang, Insights into current limitations of density functional theory, *Science*, 2008, **321**(5890), 792–794.

71 W. M. C. Foulkes, L. Mitas, R. J. Needs and G. Rajagopal, Quantum Monte Carlo simulations of solids, *Rev. Mod. Phys.*, 2001, **73**(1), 33–83.

72 B. M. Austin, D. Y. Zubarev and W. A. Lester Jr., Quantum Monte Carlo and related approaches, *Chem. Rev.*, 2012, **112**(1), 263–288.

73 J. B. Anderson, *Quantum Monte Carlo: Origins, development, applications*, Oxford University Press, 2007.

74 P. Ganesh, J. Kim, C. Park, M. Yoon, F. A. Reboredo and P. R. Kent, Binding and diffusion of lithium in graphite: quantum monte carlo benchmarks and validation of van der Waals density functional methods, *J. Chem. Theory Comput.*, 2014, **10**(12), 5318–5323.

75 J. Kim, A. D. Baczewski, T. D. Beaudet, A. Benali, M. C. Bennett, M. A. Berrill, N. S. Blunt, E. J. L. Borda, M. Casula, D. M. Ceperley and S. Chiesa, QMCPACK: An open source ab initio quantum Monte Carlo package for the electronic structure of atoms, molecules and solids, *J. Phys.: Condens. Matter*, 2018, **30**(19), 195901.

76 P. R. Kent, A. Annaberdiyev, A. Benali, M. C. Bennett, E. J. Landinez Borda, P. Doak, H. Hao, K. D. Jordan, J. T. Krogel,

I. Kylänpää and J. Lee, QMCPACK: Advances in the development, efficiency, and application of auxiliary field and real-space variational and diffusion quantum Monte Carlo, *J. Chem. Phys.*, 2020, **152**(17), 174105.

77 R. J. Le Roy, Y. Huang and C. Jary, An accurate analytic potential function for ground-state N_2 from a direct-potential-fit analysis of spectroscopic data, *J. Chem. Phys.*, 2006, **125**, 164310.

78 R. J. Le Roy, N. S. Dattani, J. A. Coxon, A. J. Ross, P. K. Crozet and C. Linton, Accurate analytic potentials for Li_2 from 2 to 90 Å, and the radiative lifetime of Li(2p), *J. Chem. Phys.*, 2009, **131**, 204309.

79 P. Giannozzi, S. Baroni, N. Bonini, M. Calandra, R. Car, C. Cavazzoni, D. Ceresoli, G. L. Chiarotti, M. Cococcioni, I. Dabo and A. Dal Corso, QUANTUM ESPRESSO: A modular and open-source software project for quantum simulations of materials, *J. Phys.: Condens. Matter*, 2009, **21**(39), 395502.

80 P. Giannozzi, O. Andreussi, T. Brumme, O. Bunau, M. B. Nardelli, M. Calandra, R. Car, C. Cavazzoni, D. Ceresoli, M. Cococcioni and N. Colonna, Advanced capabilities for materials modelling with Quantum ESPRESSO, *J. Phys.: Condens. Matter*, 2017, **29**(46), 465901.

81 H. J. Monkhorst and J. D. Pack, Special points for Brillouin-zone integrations, *Phys. Rev. B: Condens. Matter Mater. Phys.*, 1976, **13**(12), 5188–5192.

82 M. Burkatzki, C. Filippi and M. Dolg, Energy-consistent pseudopotentials for quantum Monte Carlo calculations, *J. Chem. Phys.*, 2007, **126**(23), 234105.

83 M. Burkatzki, C. Filippi and M. Dolg, Energy-consistent small-core pseudopotentials for 3 d-transition metals adapted to quantum Monte Carlo calculations, *J. Chem. Phys.*, 2008, **129**(16), 164115.

84 C. W. Greeff and W. A. Lester Jr, A soft Hartree–Fock pseudopotential for carbon with application to quantum Monte Carlo, *J. Chem. Phys.*, 1998, **109**(5), 1607–1612.

85 Additional results and discussion can be found in the ESI† to the present paper.

86 P. R. Herman, P. E. LaRocque and B. P. Stoicheff, Vacuum ultraviolet laser spectroscopy. V. Rovibronic spectra of Ar_2 and constants of the ground and excited states, *J. Chem. Phys.*, 1988, **89**, 4535–4549.

87 G. Herzberg and K. P. Huber, *Molecular Spectra and Molecular Structure: Constants of Diatomic Molecules*, Van Nostrand Reinhold Company, New York, 1979.

88 B. Kleman and S. Lindkvist, The band spectrum of the Cu_2 molecule, *Arkiv Fysik*, 1954, **8**(4), 333–339.

89 N. Aslund, R. F. Barrow, W. G. Richards and D. N. Travis, Rotational analysis of bands of b-x system of Cu_2 and a-x system of Bi_2, *Arkiv Fysik*, 1965, **30**(2), 171–185.

90 S. Grimme, Semiempirical GGA-type density functional constructed with a long-range dispersion correction, *J. Comput. Chem.*, 2006, **27**(15), 1787–1799.

91 J. N. Murrell, S. Carter, S. C. Farantos, P. Huxley and A. J. C. Varandas, *Molecular Potential Energy Functions*, Wiley, 1984.

92 A. B. Weaver and A. A. Alexeenko, Revised variable soft sphere and Lennard-Jones model parameters for eight common gases up to 2200 K, *J. Phys. Chem. Ref. Data*, 2015, **44**, 023103.

93 F. Pirani, S. Brizi, L. F. Roncaratti, P. Casavecchia, D. Cappelletti and F. Vecchiocattivi, Beyond the Lennard-Jones model: A simple and accurate potential function probed by high resolution scattering data useful for molecular dynamics simulations, *Phys. Chem. Chem. Phys.*, 2008, **10**, 5489–5503.

94 Masses of atoms are chosen to be equal to standard atomic weights according to the NIST database, **https://www.nist.gov/pml/atomic-weights-and-isotopic-compositions-relative-atomic-masses**.

95 The tables of the deflection angle can be downloaded from **http://volkov.eng.ua.edu/index.html** or obtained from the corresponding author of the present paper upon a reasonable request.

96 E. L. Tipton, R. V. Tompson and S. K. Loyalka, Chapman-Enskog solutions to arbitrary order in Sonine polynomials II: Viscosity in a binary, rigid-sphere, gas mixture, *Eur. J. Mech. B-Fluids*, 2009, **28**, 335–352.